

Thresholded Power Law Size Distributions of Instabilities in Astrophysics

Markus J. Aschwanden¹

¹) *Lockheed Martin, Solar and Astrophysics Laboratory, Org. A021S, Bldg. 252, 3251 Hanover St., Palo Alto, CA 94304, USA; e-mail: aschwanden@lmsal.com*

ABSTRACT

Power law-like size distributions are ubiquitous in astrophysical instabilities. There are at least four natural effects that cause deviations from ideal power law size distributions, which we model here in a generalized way: (1) a physical threshold of an instability; (2) incomplete sampling of the smallest events below a threshold x_0 ; (3) contamination by an event-unrelated background x_b ; and (4) truncation effects at the largest events due to a finite system size. These effects can be modeled in simplest terms with a “thresholded power law” distribution function (also called generalized Pareto [type II] or Lomax distribution), $N(x)dx \propto (x + x_0)^{-a}dx$, where $x_0 > 0$ is positive for a threshold effect, while $x_0 < 0$ is negative for background contamination. We analytically derive the functional shape of this thresholded power law distribution function from an exponential-growth evolution model, which produces avalanches only when a disturbance exceeds a critical threshold x_0 . We apply the thresholded power law distribution function to terrestrial, solar (HXRBS, BATSE, RHESSI), and stellar flare (Kepler) data sets. We find that the thresholded power law model provides an adequate fit to most of the observed data. Major advantages of this model are the automated choice of the power law fitting range, diagnostics of background contamination, physical instability thresholds, instrumental detection thresholds, and finite system size limits. When testing self-organized criticality models, which predict ideal power laws, we suggest to include these natural truncation effects.

Subject headings: Sun: flares — stars: flare — instabilities — methods: statistical

1. INTRODUCTION

Power law-like size distributions of extreme events have been discovered over the last 30 years in a large number of astrophysical phenomena in many wavelengths, such as hard X-ray and gamma-ray bursts from solar and stellar flares, auroral emission and geomagnetic substorms from planetary magnetospheres, particle events from radiation belts, pulsar glitches, soft gamma-ray repeaters, blazars, black-hole objects, cosmic rays, to boson clouds (for a recent review see Aschwanden et al. 2015 and references therein).

A unifying concept to explain and model these observed power law distributions is the concept of *self-organized criticality (SOC)* in slowly-driven nonlinear dissipative systems, originally proposed by Bak, Tang and Wiesenfeld (1987; BTW) and Katz (1986). The SOC concept is a very interdisciplinary subject, being applied in astrophysics (Aschwanden et al. 2015), geophysics (Turcotte 1999), as well as in financial physics (Feigenbaum 2003), and social sciences (Galam 2012). On the most general level, the common denominator of all SOC processes in different science disciplines is the statistics of scale-free nonlinear processes, which can be characterized by a nonlinear growth phase, during which coherent growth is enabled and has multiplicative characteristics, in contrast to linear processes with incoherent and additive characteristics. Incoherent random processes exhibit binomial, Gaussian, Poissonian, or exponential distribution functions,

while coherent processes exhibit scale-free power law-like distributions. This is the fundamental property that earthquakes, solar flares, or stock market crashes have in common, although the underlying physical mechanisms are fundamentally different. SOC behavior can also be simulated by mathematical rules, as it is demonstrated with cellular automaton models (Pruessner 2012). Consequently, there is both (i) an universally valid statistical aspect of SOC systems that leads to scale-free power law-like size distributions, and (ii) physical scaling laws that are specific to each particular SOC phenomenon. Physical scaling laws can often be expressed in terms of variables that are coupled to each other in a multiplicative way by (nonlinear) exponents, from which the power law slopes of the observed size distributions can be calculated.

Power law size distributions are the hallmarks of self-organized criticality (SOC) systems, and therefore the determination of the power law slope α is an important quest, but power law fitting is not trivial because of a number of deviations that are not properly understood. While the standard SOC models call for an ideal power law distribution function, it was rigorously proven with maximum likelihood fitting methods with goodness-of-fit tests based on the Kolmogorov-Smirnov statistic that most observed size distributions of empirical data are not consistent with an ideal power law, a power law with a cutoff, an exponential, a stretched exponential, or a log-normal distribution function (Clauset et al. 2009). Some sceptics went even as far as to deny the existence of power laws at all (Stumpf and Porter 2012). Here we propose to add a threshold constant to the ideal power law function, which describes a physical threshold, an instrumental sampling threshold, or a background contamination, which appears to fit a large number of observed (power law-like) size distributions. The introduction of a threshold constant allows us to fit an observed size distribution over a larger range without having to make any assumption of an arbitrarily chosen scale-free range over which a power law can be fitted. We will test this concept with terrestrial, solar, and astrophysical data sets, some of them investigated previously (Clauset et al. 2009; Aschwanden et al. 2015). We use the term *thresholded power law size distribution* throughout the paper, which is also known in the statistical literature as “*Generalized Pareto distribution*” (Hosking and Wallis 1987), “*Generalized Pareto Type II distribution*” (e.g., Arnold 2015; Johnson et al. 1994), or “*Lomax distribution*” (Lomax 1954).

This paper is organized into a theoretical section on the definition of thresholded size distributions, for differential and cumulative occurrence frequency distributions (Section 2), a description of the data analysis method (Section 3), analysis of terrestrial, solar, and astrophysical data sets (Section 4), a discussion of the results (Section 5), and conclusions (Section 6).

2. THEORY

2.1. Instabilities in Astrophysical Plasmas

Virtually all nonlinear energy dissipation processes in astrophysics are governed by some instability, which all have a distinct threshold. These systems are stable as long as the conditions remain below some critical threshold, while the onset of an instability is triggered when a critical threshold is locally exceeded. We list a selection of common stabilities that occur in solar and astrophysical plasmas in Table 1, and visualize their physical mechanisms in Fig. 1, including mostly hydrodynamic, magneto-hydrodynamic, and kinetic instabilities (for references see textbooks, e.g., Krall and Trivelpiece 1971; Cowling 1976; Schmidt 1979; Melrose 1980a,b, 1986; Priest 1982; Benz 1993; Sturrock 1994; Kivelson and Russell 1995; Baumjohann and Treumann 1996; Treumann and Baumjohann 1997; Somov 2000; Priest and Forbes 2000; Biskamp 2000; Tajima and Shibata 2002; Goossens 2003; Aschwanden 2004; Bellan 2006).

For the onset of an instability to be triggered (Fig. 2 left), the threshold condition could be a critical

density gradient (Rayleigh-Taylor instability), a critical velocity gradient (Kelvin-Helmholtz instability), a critical Lorentz force (ballooning instability, resistive instabilities, current pinch instabilities), a critical temperature gradient (thermal instabilities), or a critical gradient in the particle velocity distribution (bump-in-tail, two-stream, or loss-cone instabilities).

These instabilities play a fundamental role for the generation of most astrophysical phenomena, such as the formation of supermassive black holes triggered by a global dynamical instability (Begelman et al. 2006), the formation of galactic dark matter structures by a gravitational instability (Springel et al. 2005), star formation by a gravitational instability (Wang and Silk 1994), giant planet formation by a gravitational instability (Boss 1997), solar flares by magnetic reconnection instabilities (Priest and Forbes 2000), such as by the kink-mode or tearing mode instability, solar radio bursts by wave-particle interactions and kinetic instabilities (Benz 1993), coronal loop evolution by thermal instabilities (Priest 1978), auroral kilometric radiation bursts from planets by the electron-cyclotron loss-cone instability (Wu and Lee 1979), or magnetospheric substorms by velocity shear-related instabilities (Lui 1991).

Since instabilities cannot occur without crossing a critical threshold, instability thresholds are an essential ingredient in the statistical distributions of observed astrophysical (or terrestrial) phenomena. In the next section we present a simple analytical model that predicts the statistical distribution of phenomena that are subject to an instability that operates above some physically defined threshold value.

2.2. Thresholded Exponentially Growing Instabilities

There is a simple analytical model of nonlinear processes in terms of an exponential growth phase with saturation after a random time interval, which goes back to Willis and Yule (1922) who applied it to geographical distributions of plants and animals. Yule’s model was also applied to cosmic rays (Fermi 1949), to cosmic transients and solar flares (Rosner and Vaiana 1978; Aschwanden et al. 1998), or to the growth dynamics of the world-wide web (Huberman and Adamic 1999), as well as to the distribution of the sizes of incomes, cities, internet files, biological taxa, and gene and protein families (Reed and Hughes 2002). The time evolution of an exponentially growing avalanche starts at a threshold value x_0 at time $t = 0$,

$$x(t) = x_0 \left[\exp \left(\frac{t}{t_G} \right) - 1 \right] , \quad (1)$$

where t_G represents the exponential growth time. The size of the avalanche is normalized to zero for avalanches starting at time $t = 0$. If the exponential growth process saturates after a random time interval t , the statistical probability can be approximated with an exponential distribution function,

$$N(t)dt = \frac{n}{t_S} \exp \left(-\frac{t}{t_S} \right) dt , \quad (2)$$

where t_S represents the e-folding saturation time. We can now invert Eq. (1) to obtain the time dependence, $t(x) = t_G \ln(x/x_0 + 1)$, and the derivative $dt/dx = (t_G/x_0)(x/x_0 + 1)^{-1}$, and directly obtain the size distribution $N(x)$ of exponentially growing avalanches,

$$N(x)dx = N(t[x]) \left| \frac{dt}{dx} \right| dx = \frac{n(\alpha_x - 1)}{x_0} \left(\frac{x}{x_0} + 1 \right)^{-\alpha_x} dx , \quad (3)$$

where the power law index has the solution

$$\alpha_x = \left(1 + \frac{t_G}{t_S} \right) . \quad (4)$$

A more detailed discussion of this exponential-growth model can be found in Aschwanden (2011c; §3.1).

The size distribution $N(x)$ specified in Eq.(3) can be written as,

$$N(x)dx = n_0 (x_0 + x)^{-\alpha_x} dx , \quad (5)$$

with the normalization constant n_0 for the range $x_1 \leq x \leq x_2$,

$$n_0 = n_{ev}(1 - \alpha_x) [(x_2 + x_0)^{1-\alpha_x} - (x_1 + x_0)^{1-\alpha_x}]^{-1} . \quad (6)$$

This size distribution (Eq. 5) is identical to a “*Generalized Pareto distribution*” (Hosking and Wallis 1987), the “*Generalized Pareto Type II distribution*” (e.g., Arnold 2015; Johnson et al. 1994), or “*Lomax distribution*” (Lomax 1954), to which we refer as *thresholded power law size distribution* in the remainder of this Paper. Such a distribution function is also called a *differential occurrence frequency distribution function*, a *log(N)-log(S)* diagram, or simply a *size distribution*.

The ideal power law (or Pareto) distribution function of a parameter x , with a power law coefficient α_x that extends over a scale-free range of $x_1 \leq x \leq x_2$, can be retrieved from the generalized Pareto distribution simply by setting $x_0 = 0$ in Eq. (5)

$$N(x)dx = n_0 x^{-\alpha_x} dx , \quad x_1 \leq x \leq x_2 , \quad (7)$$

with n_0 being the normalization constant,

$$n_0 = n_{ev}(1 - \alpha_x) [x_2^{1-\alpha_x} - x_1^{1-\alpha_x}]^{-1} . \quad (8)$$

2.3. Cumulative Distribution Functions

For small samples, a *cumulative distribution function (CDF)* is often fitted instead, because the small number of events is not sufficient to bin the data. A cumulative size distribution is simply defined by the integral of the total number of events above a given value x , where x_1 represents the minimum value and x_2 the maximum value of the size distribution, over which the CDF is integrated. For the ideal power law distribution function (Eq. 7) we have,

$$N_{cum}(> x) dx = \int_x^{x_2} n_0 x^{-\alpha_x} dx = 1 + (n_{ev} - 1) \left(\frac{x_2^{1-\alpha_x} - x^{1-\alpha_x}}{x_2^{1-\alpha_x} - x_1^{1-\alpha_x}} \right) . \quad (9)$$

where n_{ev} is the total number of events included in the size distribution. Strictly speaking, this definition is only valid for exponents $\alpha_x \neq 1$, while the integral takes on the form of $\propto \ln(x)$ for $\alpha_x = 1$. Note that this distribution has an asymptotic value of $N_{cum}(> x_1) = n_{ev}$ at the lower bound, and vanishes at the upper bound, $N_{cum}(> x_2) = 0$. It is important to note that the cumulative size distribution (Eq. 9) is not exactly a power law function with a slope of $\beta = \alpha - 1$, but rather shows a steep drop-off at the upper end like an exponential function, due to the highest value that forces the probability to vanish above x_2 . It is a consequence of the fact that the differential size distribution has a sharp upper bound at x_2 and does not continue to infinity, an effect that is also called a *finite system size effect* in SOC models. This deviation from a straight power law (of the cumulative size distribution) is often ignored, or is modeled with an *ad hoc* (exponential) term, i.e., $N(x)dx \propto x^{-\alpha_x} \exp(-x/x_0)$ (e.g., Lu et al. 1993), but we will fit it properly to the data in this study by fitting the exact analytical distribution function defined in Eq. (9) (see examples in Figs. 3c and 3d).

The thresholded size distribution has the following CDF,

$$N_{cum}(> x) = \int_x^{x_2} n_0(x + x_0)^{-\alpha_x} dx = 1 + (n_{ev} - 1) \left(\frac{(x_2 + x_0)^{1-\alpha_x} - (x + x_0)^{1-\alpha_x}}{(x_2 + x_0)^{1-\alpha_x} - (x_1 + x_0)^{1-\alpha_x}} \right) . \quad (10)$$

The bounds $[x_1, x_2]$ and the number of events n_{ev} are known in principle, which leaves two free variables (x_0, α) . From the definition given in Eq. (10) we see immediately that the cumulative size distribution obtains the value $N_{cum}(> x_1) = n_{ev}$ at the lower bound $x = x_1$, and $N_{cum}(\geq x_2) = 1$ at the upper bound $x = x_2$. A set of differential size distributions $N(x)$ (for $x_0 = 0, 10, 20, \dots, 50$) is shown in Fig. (3b), as well as the corresponding set of cumulative size distributions $N(> x)$ (Fig. 3d). Further examples of such size distributions with different power law slopes $\alpha_x = 1.0, 1.2, \dots, 3.0$ are shown in Fig. (4b) and (4d).

2.4. Truncation Effects due to Incomplete Sampling

The low end of a power law-like distribution function often shows a deviation from an ideal power law function in form of a gradual rollover, which is caused by undersampling below the detection threshold. The detection threshold is a different physical cause than the instability threshold x_0 derived in Section 2.2, but can be mathematically treated in the same way. Therefore, the (positively-defined) parameter $x_0 > 0$ in the thresholded size distribution (Eq. 5) has a double meaning, it could be caused by the physical threshold of the relevant instability, or it could be caused by the finite sensitivity of an instrument. This ambiguity can only be resolved by using additional information. For instance, if a data set with higher sensitivity is used, the value x_0 should move to lower values (Fig. 2 right), while it should stay constant for a physical instability threshold that is instrument-independent (see effect of instability threshold E_{T0} and detection threshold E_{D0} on cumulative size distribution in Fig. 2 right panel).

2.5. Background Contamination

Actually, the parameter x_0 has a third meaning, if it is negative, $x_0 < 0$. In any size distribution of a certain type of events, it is always possible to have an event-unrelated background that is responsible for false detections at the level of the smallest events. In particular in astrophysical data sets, the flux $f(t)$ of events that is sampled may often contain some event-unrelated background $b(t)$, so that the total observed flux $F(t) = f(t) + b(t)$ represents an over-estimate of the event-related flux $f(t)$. For instance, hard X-ray pulses originating from solar flares always contain some background photons of the same energy that originate from non-solar sources (such as the galactic background). Such a background contamination effect has the same functional form as a thresholded power law distribution function (Eq. 5),

$$N(x)dx = n_0(x + x_0)^{-\alpha_x} dx = n_0(x - b_0)^{-\alpha_x} dx , \quad (11)$$

except that the offset constant $x_0 = -b_0$ is negative. A set of differential size distributions $N(x)$ (for $x_0 = 0, 10, 20, \dots, 50$) is shown in Fig. (3a), as well as the corresponding set of cumulative size distributions $N(> x)$ (Fig. 3c). Further examples of such size distributions for different power law slopes $\alpha_x = 1.0, 1.2, \dots, 3.0$ are shown in Fig. (4a) and (4c). We see that the lower end of the size distributions show a steepening of the power law slope, while a cutoff occurs at $x = b_0$. In practice, the background b_0 may not be a constant value for each event, but for sake of simplicity we study here only the zero-order effect of a constant background value.

3. NUMERICAL METHODS

After we described the theoretical framework of thresholded power law distributions (Section 2.2, 2.3), and the effect of incomplete sampling (Section 2.4) and background contamination (Section 2.5), we turn now to the numerical method to fit these modified power law distribution functions to data sets and to evaluate a goodness-of-fit criterion. We will use Monte-Carlo simulations to validate the numerical method used here.

3.1. Monte-Carlo Simulations of Power Law Distributions

We start with Monte-Carlo simulations of generalized (thresholded) power law distributions of the form of Eq. (5). We wish to generate a data set $x_i, i = 1, \dots, n$ as a function of random numbers ρ_i that are drawn from a random generator in the range of $\rho_i = [0, 1]$, and produce a size distribution function $N(x)$ as prescribed by Eq. (5). The general procedure to set up such a Monte Carlo simulation is described in some detail in Clauset et al. (2009; Appendix D) or Aschwanden (2011c; §7.1.4). First we normalize the differential probability function to unity,

$$p(x) = \frac{N(x)}{n_{ev}} = \frac{n_0}{n_{ev}}(x + x_0)^{-\alpha_x}, \quad (12)$$

and obtain the total probability distribution function $P(x)$ integrated over the range $[x_1, x]$,

$$P(x) = \int_{x_1}^x p(x') dx' = \left(\frac{(x + x_0)^{1-\alpha_x} - (x_1 + x_0)^{1-\alpha_x}}{(x_2 + x_0)^{1-\alpha_x} - (x_1 + x_0)^{1-\alpha_x}} \right), \quad (13)$$

and set it equal to the (normalized) sorted random values $\rho_i = [0, 1]$,

$$P(x) = \int_{x_1}^x p(x') dx' = \int_0^\rho d\rho' = \rho, \quad (14)$$

which yields a relationship between the sizes x_i and random values ρ_i and can explicitly be expressed as a function $x(\rho)$ by the inversion of the total probability distribution function (Eqs. 13, 14),

$$x(\rho) = [\rho(x_2 + x_0)^{1-\alpha_x} + (1 - \rho)(x_1 + x_0)^{1-\alpha_x}]^{1/(1-\alpha_x)} - x_0. \quad (15)$$

This numerical procedure allows us to simulate the generalized power law distribution functions with different random number sets, by using a random generator to produce values $\rho_i = [0, 1]$ that map into the size range $x_i = [x_1, x_2]$ and reproduce the probability distribution function of Eq. 12). Such Monte-Carlo simulations provide uncertainties of the power law size distribution parameters (α_x, n_0, x_0) due to random noise, which can be used to calculate a χ^2 goodness-of-fit criterion that tells us which of the observed distributions are consistent with the theoretical model of a thresholded power law distribution function (Eq. 5).

3.2. Least-Square Goodness-of-Fit Test

We simulate 10 different data sets with $x_0 = 10$, $a = 2.0$, with different numbers of events, $n_{ev} = 10^5 \times 2^{(-i)}$, $i = 1, \dots, 10$. Each one has uniformly distributed random numbers $\rho_i, i = 1, \dots, n_{ev}$ from a range of unity $\rho_i = [0, 1]$. We transform the values ρ_i into size variables $x_i(\rho_i)$ according to the function of Eq. (15),

and sample them in $n_x = 40$ uniform logarithmic bins in the range of $x_i = [1, 10^5]$. We show the resulting differential size distributions $N(x)$ (Fig. 5a) and cumulative size distributions (Fig. 5c). The counted number of events per bin in the differential size distribution function is $N_{bin,i}$, while the differential distribution function is defined by dividing with the (non-equidistant) bin width Δx_i , so that $N_i(x_i) = N_{bin,i}(x_i)/\Delta x_i$. The expected uncertainty of the differential size distribution is then

$$\sigma_{diff,i} = \sqrt{(N_i \Delta x_i)/\Delta x_i}, \quad (16)$$

while the expected uncertainty of the cumulative size distribution, which we represent with the same (logarithmic) binning, is

$$\sigma_{cum,i} = \sqrt{N_i}. \quad (17)$$

We can now calculate a goodness-of-fit χ^2 -criterion for the difference between the simulated distributions $N_{sim,diff}(x)$ and the theoretical distribution function $N_{fit,diff}$ for both the differential size distribution function (with $n_{par} = 3$ parameters, a, x_0, n_0),

$$\chi_{diff} = \sqrt{\frac{1}{(n_x - n_{par})} \sum_{i=1}^{n_x} \frac{[N_{fit,diff}(x_i) - N_{sim,diff}(x_i)]^2}{\sigma_{diff,i}^2}}, \quad (18)$$

and the cumulative distribution function $N_{fit,cum}(x)$,

$$\chi_{cum} = \sqrt{\frac{1}{(n_x - n_{par})} \sum_{i=1}^{n_x} \frac{[N_{fit,cum}(x_i) - N_{sim,cum}(x_i)]^2}{\sigma_{cum,i}^2}}, \quad (19)$$

which are both shown in Figs. (5b) and (5d), together with error bars based on 1000 different realizations of random number sets. This test shows clearly that the defined goodness-of-fit criterion yields the expected value of $\chi^2 \approx 1.0$ for pure random noise. The statistical averages are $\chi^2 = 1.05 \pm 0.02$ for the differential size distributions (Fig. 5b), and $\chi^2 = 0.82 \pm 0.01$ for the cumulative size distributions (Fig. 5d). The latter value deviates from the expectation value of χ^2 due to the statistical dependence of the counts in binned cumulative size distribution, but is close enough to unity to serve as a sensible goodness-of-fit criterion.

Note that the events in each bin of the differential size distribution are statistically independent, while the number of events $N_{cum}(x)$ in the cumulative size distribution are statistically dependent. However, since we use a fixed (logarithmic) binning, the fluctuations of events in each bin, $N_{cum}(x) = \int_x^{x^2}$, obey approximately the same random statistics $\sigma_{cum,i} = \sqrt{N_{cum,i}}$ in each bin as for the differential size distribution, $\sigma_{diff,i} = \sqrt{N_{diff,i}}$, so that we have uncertainty estimates $\sigma_{diff,i}$ (Eq. 16) and $\sigma_{cum,i}$ (Eq. 17) for both distributions and can apply the goodness-of-fit criteria χ_{diff} (Eq. 18) and χ_{cum} (Eq. 19) for both types of distributions, as proven in Fig. (5b) and (5d).

3.3. Fitting of Power law Distributions

In the following data analysis, the simulated distributions will be replaced by the distributions of the observed data, $N_{sim}(x) \mapsto N_{obs}(x)$, while the theoretical distribution function will be replaced by the actual best fit of the theoretical model, $N_{fit}(x)$. Calculating the goodness-of-fit χ^2 criteria (Eqs. 18, 19) will tell us whether the data are consistent with the theoretical model (Eq. 5) or not.

Alternative methods to the least-square fit test are maximum likelihood estimators for generalized Pareto distributions (Goldstein 2004; Newman 2005; Bauke 2007; Giles et al. 2011), the Bayesian information

criterion (BIC), the Kolmogorov-Smirnov (KS) test, or the Anderson-Darling (AD) test, which have been applied to the cumulative size distributions of empirical data sets in Clauset et al. (2009). In the latter application, the KS test was considered to yield good results, while the AD test was found to give estimates of the lower bound x_1 (of the power law range in the cumulative size distribution) that are too large by an order of magnitude or more, while the BIC method was found to have a tendency of underestimating x_1 (Clauset et al. 2009). Since our Monte-Carlo simulations validated the χ^2 minimization goodness-of-fit test for both the differential (Fig. 5b) and cumulative size distribution (Fig. 5d), we will use this method throughout this study.

Our data analysis procedure of fitting thresholded power law size distributions to the data and evaluating the goodness-of-fit comprises the following steps: (1) histogram binning of both the differential and cumulative size distributions; (2) determination of the threshold value x_0 ; (3) optimization of the free parameters n_0 and a and least-square goodness-of-fit test; and (4) elimination of event-unrelated background contamination. We briefly describe these four steps in turn.

Step 1: Histogram binning: The input from every data set is a series of event sizes $x_i, i = 0, \dots, n_{ev}$ with a total of n_{ev} events. This series is defined by a minimum $x_1 = \min(x_i)$ and maximum value $x_2 = \max(x_i)$. We apply a logarithmic binning to the data for both the differential and the cumulative size distributions, which is uniform on a logarithmic scale and covers the sampled data range $[x_1, x_2]$. For differential size distributions we use $n_{dec} = 10$ logarithmic bins per decade, yielding $n_{bin} = {}^{10} \log(x_2/x_1) \times n_{dec}$ bins per data set, while we use $n_{dec} = 5$ logarithmic bins per decade for cumulative size distributions. Bins without events in the differential size distribution (which show no change in the number of events in the cumulative size distribution) are ignored.

Step 2: Threshold x_0 : Since the lower end of the (differential or cumulative) size distribution is often subject to incomplete sampling, it is necessary to find a lower bound or threshold x_0 that defines an upper range $[x_0, x_2]$ where events are completely sampled and a power law fit can be applied. We find that a reliable lower bound x_0 can be determined from the bin where the number of events per bin has a maximum,

$$N_{diff,max} = \max[N_{diff}(x)] = N_{diff}(x = x_0) . \quad (20)$$

We show an example in Fig. (6), where the peak counts of a data set of 10,665 solar flares are sampled in form of a logarithmically binned histogram (with data taken from Clauset et al. 2009). The number of events $N_{bin,i}$ per (logarithmic) bin is shown in Fig. (6a), where the maximum of the distribution defines the threshold value x_0 . The resulting differential size distribution is obtained from dividing the number of events per bin by the (logarithmic) bin width, $N_{diff}(x) = N_{bin,i}/\Delta x_i$ (Fig. 6b), and the cumulative distribution function is obtained from the the number of events in the integrated ranges $[x, x_2]$, namely $N_{cum}(> x_i) = \int_x^{x_2} N_{diff,i}(x) dx$ (Fig. 6c).

The rationale for this method of finding a lower threshold x_0 is justified as follows. For an ideal power law distribution that is completely sampled over the entire range $[x_1, x_2]$, we would expect that the number of events per bin monotonically increases towards the lower bound, $x \mapsto x_1$, for power law slopes steeper than $a > 1$, such as shown in the simulation for $a = 2.0$ in Fig. (5c.) In real data, the lower range is generally sampled incompletely (unless we have a 100% detection efficiency all the way down the size of the smallest event in the data set). Therefore, if we find a decrease in the number of events per bin when moving towards the lower bound, say in the range $x_1 \leq x \leq x_0$, this decrease in events indicates undersampling, or an incompletely sampled range, and thus it is appropriate to limit the fitting range to the completely sampled range $[x_0, x_2]$.

Step 3: Optimization of the free parameters n_0 and α : Fitting the theoretical function (Eq. 5) to the data involves three free variables, the threshold x_0 , the normalization constant n_0 , and the power law slope a . In principle, the constant n_0 is known from the normalization to the total number of events in the data set, n_{ev} (Eq. 6), but this is only true for completely sampled data sets where the threshold coincides with the data minimum value ($x_0 = x_1$), such as in the data simulations shown in Figs. 3 and 4. Since the threshold x_0 is already determined in the previous step, we have only two free variables (n_0 and α) to optimize, which we obtain by means of minimizing the χ^2 -values (Eqs. 18 and 19) that express the least square difference between the theoretical model $N_{fit}(x_i)$ (Eq. 5) and the histogrammed data points $N_{obs}(x_i)$, $i = 0, \dots, n_{bin}$. We perform the optimization of the χ^2 -values by using a Powell minimization method (Press et al. 1986). The resulting χ^2 -values provide also a goodness-of-fit test, whether the model fits the data (in case of $\chi^2 \approx 1$). Values of χ^2 significantly above unity indicate a failure of the model fit, while values significantly below unity indicate noisy data that are not sensitive to the model fit.

Note that the fitted parameter a corresponds to an effective slope $b = a - 1$ for the cumulative size distribution. We estimate an error σ_a of the fitted power law slope a from a relationship that scales with the square root of the number n of events and was derived earlier from Monte-Carlo simulations (Aschwanden 2011a),

$$\sigma_\alpha = \frac{\alpha}{\sqrt{n}}. \quad (21)$$

which is slightly different from the definition obtained with maximum likelihood estimators in generalized Pareto distributions (e.g., in Clauset et al. 2009), $\sigma_\alpha = (\alpha - 1)/\sqrt{n}$. Thus we expect an accuracy of approximately 10% for $n = 100$ events, or 1% for $n = 10^4$ events.

Step 4: Elimination of event-unrelated background: If the data reveal a steepening of the power law slope near the threshold value x_0 , such as shown in Fig. (3a) or (3c), this indicates the presence of event-unrelated background contamination. To first order, we can correct for this effect by subtracting a suitable background value b_0 , i.e., $x_{corr} = x - b_0$. If the background value b_0 would be an exact constant, a sharp lower cutoff at $x = b_0$ would occur in the size distributions, such as shown in the Monte-Carlo simulations in Figs. (3a,3c) or in Figs. (4a,4c). In reality, there are events with values of $x < b_0$ in the sample, which become negative after correction and get lost from a positively defined size distribution. Since we are only interested in a corrected power law slope above a threshold value $x_0 > x_b$, we ignore negative values after correction, but we have to be aware that this reduces the overall number of sampled events.

In the absence of information on the correct background value for each event, the question arises how can we determine a mean value b_0 empirically? As the Monte-Carlo simulations in Figs. 3 and 4 show, the size distributions with a steepening at the lower end converge to the extrapolated power law slope, when the correct background is subtracted. Therefore, we can find the correct mean background value by varying the values $x_0 = -b_0$ in the fitted thresholded power law function (Eq. 5) until the χ^2 -values reach a minimum. We demonstrate this procedure in Fig. (7). A differential size distribution is shown for an observed data set of 10,665 solar flares (taken from Clauset et al. 2009), with no background subtraction (Fig. 7a), which shows a clear discrepancy between the best fit of a thresholded power law function and the power law slope at the upper bound, which is interpreted as an effect of unsubtracted background that steepens the distribution at the lower end. The resulting goodness-of-fit with no background subtraction, $\chi^2 \approx 6$ (Fig. 7d), clearly indicates a bad fit. If we increase the level of background subtraction, the goodness-of-fit improves and reaches a best value of $\chi^2 \approx 1.0$ at a background level of $b_0 = 57 \text{ cts s}^{-1}$ (Fig. 7b and 7d). The goodness-of-fit remains at a similar level for subtraction of larger backgrounds ($b_0 = 57 - 120$), because no background contamination occurs at larger events than $x \geq b_0$. After we have determined the correct background b_0 , step 3 is repeated to obtain optimum values for the parameters n_0 and a of the background-subtracted values

$$x_{corr} = x - b_0.$$

4. DATA ANALYSIS

We are fitting our analytical model of differential and cumulative thresholded size distributions to a number of data sets from terrestrial, solar, and stellar data. The mostly terrestrial data stem from Clauset et al. (2009), the solar data have been previously reviewed in Aschwanden et al. (2015), and the stellar data are obtained from the *Kepler* mission, either from published or newly processed data. We analyze all size distributions with the same unified methodology and compare the obtained power law slopes with published values obtained with alternative methods.

4.1. Terrestrial and Empirical Data

We use 9 data sets out of the 24 empirical data sets published by Clauset et al. (2009) for two reasons: (1) Most of these data sets have large statistics in the order of $10^4 - 10^5$ events, which is needed for accurate power law fits, and (2) nine of these data sets are accessible from public websites (see URL links, description of data sets, and origin with references in Clauset et al. 2009). For all of these data sets, ideal power law functions (Eq. 7) have been fitted, a lower bound x_0 for the power law range has been determined and the power law hypothesis has been tested in Clauset et al. (2009). Alternatively, we fit here *thresholded power law distribution functions* (Eq. 5) to both differential (Fig. 8) and cumulative size distributions (Fig. 9). In addition we test the hypothesis whether thresholded power laws are consistent with the data with the χ^2 goodness-of-fit criteria. The results are summarized in Table 2.

The 9 empirical data sets selected from Clauset et al. (2009) are gathered from one solar (a), two geophysical (b,c), three social (d,e,f), and three information-type (g,h,i) statistical data sets: (a) hard X-ray peak count rates from **solar flares** observed with HXRBS/SMM (Dennis 1985; Schwartz et al. 1992; Crosby et al. 1993; Newman 2005); (b) the intensities of **earthquakes** occurring in California between 1910-1992 measured from the maximum amplitude of motion (Newman 2005); (c) the areas of **wildfires** (in units of acres) occurring on USA federal land between 1986 and 1996 (Newman 2005); (d) the human population of USA **cities** in the 2000 US Census; (e) the number of customers affected in electrical **blackouts** in the USA during 1984-2002 (D’Agostino et al. 1986); (f) the casualties of **terrorist** attacks worldwide from February 1968 to June 2006 (Clauset et al. 2007); (g) the frequency of occurrence of unique **words** in the novel *Moby Dick* by Herman Melville (Newman 2005); (h) the frequency of occurrence of US family **surnames** in the 1990 US Census; and (i) the number of **web links** to web sites found in a 1997 web crawl of about 200 million web pages (Broder et al. 2000).

If we allow a generous limit of $\chi^2 \lesssim 1.3$ for the goodness-of-fit in the cumulative size distribution, we find that 4 out of the 9 empirical data sets are consistent with the hypothesis of a thresholded power law size distribution (flares, quakes, blackouts, surnames), while the other 5 cases are inconsistent with the hypothesis (fires, cities, terrorism, words, weblinks). Clauset et al. (2009) finds support for a power law, or for a power law with cut-off, for all of these 9 cases, but the specific shape of the cutoff is not fitted and the lower bound x_0 is determined differently than in our work.

When we look at the power law slopes and their uncertainties (Table 2), we find good agreement between our differential and cumulative size distributions within the quoted uncertainties in almost all cases

(Table 2: 5th and 6th column). Comparing with the power law slopes obtained by Clauset et al. (2009), we find approximate agreement (within the stated uncertainties) for a few data sets only (flares, words, surnames, weblinks). The remaining discrepancies are mostly caused by the choice of the fitting range, which is dictated by the threshold value x_0 of complete sampling in our study, while Clauset et al. (2009) use a heuristic method. Those cases that are not consistent with the thresholded power law model, such as the cities and fires, exhibit significant deviations over a large portion of the fitting range, where a power law fit is ill-defined anyway.

Regarding background subtraction we found the largest contamination for the data set of solar flares ($b_0 = 57 \text{ cts s}^{-1}$), which includes the preflare background count rate. This is actually fairly consistent with the galactic hard X-ray background count rate for the HXRBS/SMM data set, which is estimated to produce a mean background level of $\approx 40 \text{ cts s}^{-1}$ (Dennis 1985). A minor background component of 1-2 units was found also for five other data sets (fires, terrorism, quakes, words, surnames, weblinks), which could possibly be attributed to a discretization effect (since the lowest values in these data sets are digitized by discrete integer numbers).

In summary, we find a good consistency between the power law slopes determined from the differential and cumulative size distributions, but we find substantial differences between the power law slopes determined with our χ^2 -square method and the *maximum-likelihood fitting (MLF)* method of Clauset et al. (2009), which **is caused** by differently chosen fitting ranges, rather than by the fitting method. The choice of the distribution model (e.g., ideal power law versus the thresholded power law model) appears to be more important in determining which model is most consistent with the data than the fitting method.

4.2. Solar Data

One of the most suitable data sets with power law behavior in solar physics are count rates of hard X-ray peak fluxes P from solar flares, because of their near-perfect match to a power law function, their large statistics ($\approx 10^3 - 10^5$ events per data set), multiple instrument coverage (SMM, CGRO, RHESSI), multiple solar cycle coverage (Cycle 21-24), and multiple published analyses.

Solar flares provide the energy source for acceleration of nonthermal particles, which emit bremsstrahlung in hard X-ray wavelengths, once the non-thermal particles interact with a high-density plasma via Coulomb collisions. Most solar flares display an impulsive component in hard X-rays, produced by accelerated coronal electrons that precipitate towards the chromosphere and produce intense hard X-ray emission at the foot-points of flare loops. Therefore, hard X-ray pulses are a reliable signature of solar flares, often detected at energies $\gtrsim 20 \text{ keV}$, but for smaller flares down to $\gtrsim 8 \text{ keV}$.

Solar flare event catalogs containing the peak rate (P), fluences (E), and flare durations (T), have therefore been compiled from a number of spacecraft or balloon-borne hard X-ray detectors over the last three decades, such as from OSO-7 (Datlowe et al. 1974), a University of Berkeley balloon flight (Lin et al. 1984), HXRBS/SMM (Dennis 1985; Schwartz et al. 1992; Crosby et al. 1993), BATSE/CGRO (Schwartz et al. 1992; Biesecker et al. 1993, 1994; Biesecker 1994), WATCH/GRANAT (Crosby 1996; Georgoulis et al. 2001); ISEE-3 (Lu et al. 1993; Lee et al. 1993; Bromund et al. 1995); PHEBUS/GRANAT (Perez-Enriquez and Miroshnichenko 1999). RHESSI (Su et al. 2006; Christe et al. 2008; Lin et al. 2001), and ULYSSES (Tranquille et al. 2009). A compilation of occurrence frequency distribution power law slopes of solar hard X-ray flare peak fluxes (α_P), fluences or energies (α_E), and flare durations (α_T) is listed in Table 3.

We show the fits of differential and cumulative size distributions to the HXRBS/SMM data set in Figs. 10 and 11 (top panels). The entire data set comprises 10291 events from the 1980-1989 (solar cycle 21/22) period, but the subtraction of an average background of 57 cts s^{-1} reduces the sample of peak fluxes to 7931 events. The results for the BATSE/CGRO data set from 7233 flares observed during the epoch of 1991-2000 (solar cycle 22/23) are shown in Figs. 10 and 11 (middle panels), which reveals no significant background (in the catalogued values). The results for the RHESSI data set from 11549 flare events observed during 2002-2010 (cycle 23/24) is shown in Figs. 10 and 11 (bottom panels), where we found an empirical background of 35 cts s^{-1} . For each of the three data sets we sampled three different parameters, the peak flux P , the total (time-integrated) counts E , and the time duration D , each one shown in Figs. 10 and 11. A graphic visualization of the power law slopes of the 3 solar flare parameters as a function of the size of the data set is shown in Fig. 12. We notice that most of the power law slopes are centered in the ranges of $\alpha_P \approx 1.6 - 1.9$, $\alpha_E \approx 1.4 - 1.7$, and $\alpha_D \approx 2.0 - 3.0$. The peak fluxes and total counts show generally a more pronounced power law function than the durations.

Since there is a spread of values for the power law slopes, even for the same data set analyzed by different authors (see Table 3), we investigate a few systematic effects. The variation of fitted power law slopes seems not to depend on the size of the data set, if at least $n \gtrsim 10^2$ events are sampled, as it can be seen in Fig. 12. We varied the level of background subtraction from 0 to 100 cts/s and find a strong variation of the power law slope for differential size distributions, while the cumulative size distributions appears to be less dependent on the background subtraction level (Fig. 13, top). If we vary the number of sampled flare events, we see good agreement between the slopes of cumulative versus differential size distributions for data sets that have a minimum size of $n \gtrsim 10^3$ (Fig. 13, bottom), according to the expected accuracy of the power law slope that scales as $\sigma_\alpha = \alpha/\sqrt{n}$ (Aschwanden 2011a). A slight variation of the power law slope during three solar cycles was noted also (Fig. 9 in Aschwanden 2011a), which can be explained with a variation of the energy threshold for flaring (Aschwanden 2011b).

4.3. Stellar Data

The capability of obtaining statistics of stellar flare data has been drastically enhanced recently with observations from the *Kepler Mission* (Koch et al. 2010), which provides high-precision lightcurves of individual stars in optical wavelengths. These lightcurves contain quiescent emission from a star that causes a slow sinusoidal modulation due to the star rotation, while fast bursts from stellar flares are superimposed that can accurately be measured after subtraction of the slowly modulated background (Walkowicz et al. 2011). Searches of white-light flare emission yielded data of 373 flaring cool dwarf stars in the Kepler Quarter 1 data (Walkowicz et al. 2011), 365 superflares from slowly rotating solar-type stars (Maehara et al. 2012), 1547 superflares on 279 G-type dwarfs (Shibayama et al. 2013), 209 flares from K-M flare stars and A-F stars (Balona 2015), and 4944 superflares on 77 G-type stars (Wu, Ip, and Huang 2015). We tabulate a list of power law slopes that have been measured from the size distributions of white-light flares observed with Kepler in Table 4, which are found in the range of $\alpha \approx 1.5 - 3.0$.

Our primary interest here is to test the hypothesis whether stellar flare data are consistent with our hypothesis of thresholded power law size distributions (Eq. 5). We show the differential size distributions of three large Kepler data sets ($n_{ev} \gtrsim 10^3$) and six smaller data sets from individual stars in Fig. 14, and the corresponding cumulative size distributions in Fig. 15. We find that the cumulative size distributions are all consistent with the thresholded power law size distribution model, based on a goodness-of-fit of $\chi^2 \lesssim 1.0$. The size distributions of flares from individual stars contain less statistics. We extracted the six largest data

sets, which have 37–57 flare events per star. Those data sets have larger uncertainties and provide less constraints to test the accurate power law shape. Unfortunately we were not able to find a star for which we could compare the power law slopes given in publications and calculated in this study. Nevertheless, the compilation of analyzed values for the power law slopes of stellar flares observed with Kepler (Table 4) shows similar ranges among different studies: $\alpha \approx 2.0 - 2.3$ in Maehara et al. (2012), $\alpha \approx 2.0 - 2.2$ in Shibayama et al. (2013), $\alpha \approx 1.6 - 2.1$ in Wu et al. (2015), and $\alpha \approx 1.5 - 3.2$ in this study. These values for the power law slopes obtained for stellar flares are systematically higher than for the solar flares tabulated in Table 3, but we have to be aware that the white-light (bolometric) fluxes are measured in stellar flares with Kepler, while hard X-ray fluxes are measured in solar flares with HXRBS, BATSE, and RHESSI, which may be related to each other by a nonlinear scaling relationship. Application of physical models to these measurements are beyond the scope of this paper and will be conducted elsewhere.

Considering the relatively small number statistics of stellar flares, the measurement of power law slopes is challenging, since the rollover due to undersampling causes a flattening at the lower end of the distribution, and the finite-size effect causes a steepening at the upper end of the distribution, and there is almost no intervening range where the power law slope can be reliably measured. It is therefore imperative to model and fit all three effects simultaneously.

5. DISCUSSION

5.1. The Problematics of Power Laws

Stumpf and Porter (2012) write in their article *Critical Truths About Power Laws*: “A striking feature that has attracted considerable attention is the apparent ubiquity of power law relationships in empirical data. However, although power laws have been reported in areas ranging from finance and molecular biology to geophysics and the Internet, the data are typically insufficient and the mechanistic insights are almost too limited for the identification of power law behavior to be scientifically useful.” This sceptical remark echoed similar thoughts made in an extensive study on *Power-Law Distributions in Empirical Data* (Clauset et al. 2009), from which we quote: *Unfortunately, the detection and characterization of power laws is complicated by the large fluctuations that occur in the tail of the distribution – the part of the distribution representing large but rare events – and by the difficulty of identifying the range over which power law behavior holds. Commonly used methods for analyzing power law data, such as least-square fitting, can produce substantially inaccurate estimates of parameters for power law distributions, and even in cases where such methods return accurate answers they are still unsatisfactory because they give no indication of whether the data obey a power law at all.* Clauset et al. (2009) combine maximum-likelihood fitting methods with goodness-of-fit tests based on the Kolmogorov-Smirnov statistic and likelihood ratios, and find that the hypothesis of a power law is consistent with data in some cases, while it is ruled out in other cases.

Given these problematics, we identify three major problems: (1) Insufficient statistics, (2) the definition of the fitting range, and (3) the choice of the model. The first problem can be overcome by using more sensitive instruments that can sample events down to a lower level, or by increasing the observing time span, which boosts the number of detected events proportionally to the total duration of observations. Both trends are ameliorated currently, because high-technology developments provide us with more sensitive instruments in almost all areas, and data sets are now available over decades of years, since automated measurements started around 1950. In particular for solar and astrophysical measurements, the beginning of the space age after 1956 has opened up the capabilities to sample large data sets with space-borne instruments in virtually

all wavelengths.

The second problem of defining a fitting range for power law distributions represents a methodical problem that can be solved systematically, as we demonstrate in this paper. It is true that most power law fits in the past have been carried out by eye-balling a straight portion of a size distribution on a log-log scale, and then applying a linear regression fit to the logarithmic histogram in this “scale-free” range. While such measurements with a clearly visible power law range $[x_{p1}, x_{p2}]$ are still reasonably accurate, the problem becomes ill-defined when the power law slope gradually varies from a flat segment at the lower end $[x_1]$ to a steepening edge at the upper end $[x_2]$ (for examples see Fig. 6.1 and 6.2 in Clauset et al. 2009). In principle, one could quantify the problem by subdividing a size distribution into three zones, bound by the values $x_1 \leq x_{p1} \leq x_{p2} \leq x_2$, where the middle part $[x_{p1}, x_{p2}]$ is fitted with a power law function, while the lower $[x_1, x_{p1}]$ and upper zone $[x_{p2}, x_2]$ are fitted with appropriate other model functions (as visualized in Fig. 2, right panel). However, such a method would still fail for data sets with small-number statistics, because the pure power law range $[x_{p1}, x_{p2}]$ shrinks to arbitrary small ranges (see examples of flare events for single stars (Figs. 14-15; second and third row).

The third problem, the choice of the model, is discussed in the next section, where we argue which most likely effects should be included in models of power law-like distribution functions.

5.2. Evaluating Thresholded Power Laws

The ideal solution of model fitting is always a complete model that includes all measurements or data points, quantified with a minimum number of free parameters (Occam’s razor criterion). For our size distribution fitting problem, this means that a complete model should describe not only the power law part in the range $[x_{p1}, x_{p2}]$, but also the flattening in the lower portion $[x_1, x_{p1}]$ and the steepening in the upper portion $[x_{p2}, x_2]$. We accomplish this goal simply by adding a threshold x_0 to the pure power law function, i.e., $N(x)dx = (x + x_0)^{-a}$ (Eq. 5), which serves a three-fold purpose: (1) x_0 quantifies a lower threshold above which a data set is completely sampled; (2) x_0 could represent also a critical physical threshold of an instability (in terms of an exponentially growing avalanche); and (3) $x_0 = -b_0$ can also be used to subtract an event-unrelated background b_0 from the data before fitting of a model function is applied. Furthermore, the largest event x_2 of the data set represents a sharp cutoff in the differential size distribution, which produces a gradual steepening in the cumulative size distribution (Eq. 10), which has to drop to zero for values $x > x_2$. Fitting the correctly integrated cumulative size distribution (Eq. 10) will then take care of the steepening near the upper end of the observed size distribution.

How successful is this new method of thresholded power laws? First of all, this method involves only one more free parameter (x_0) than fitting a straight power law distribution function (with two variables n_0 and a), and thus it follows Occam’s razor criterion. If we look at the 9 empirical data sets in Fig. 9, we find that a thresholded power law is consistent with the data ($\chi^2 \leq 1.6$) in 4 out of the 9 cases, for which it yields accurate power law slopes. In contrast, two cases are clearly not consistent (cities and fires), which probably could be fitted with a broken power law, indicating two different scaling regimes. Regarding the interpretation of these 9 empirical data sets, we can certainly consider solar (flares) and geophysical phenomena (earthquakes and forest fires) as thresholded instabilities, as it was proposed for self-organized criticality phenomena, while phenomena in sociophysics (city growth, power blackouts, terrorism attacks, stockmarket bubbles) have the statistics of extreme events in common, and information-type phenomena (words, surnames, weblinks) have the multiplicative behavior of combinational processes in common (such

as in branching theory or percolation processes).

For solar flare data the thresholded power law model is consistent with all data sets (HXRBS, BATSE, RHESSI) regarding the peak count rate and total counts (Fig. 11), while the size distributions for flare durations show some slight deviations, which could indicate a bimodality between short and long-duration flares. This is not surprising, because the duration of long-lasting flares (several hours) is less well-defined due to interruptions from the spacecraft orbit, and due to confusion of time-overlapping flare events.

For stellar flare data we find consistency ($\chi^2 \lesssim 1$) of the thresholded power law model for all size distributions, for stellar flares that are combined from many stars (Figs. 14-15; top row), as well as for flare events from single stars (Figs. 14-15; second and third row). This agreement is partially helped by the unavoidable small-number statistics, but it holds up to samples with 1538 flare events observed with Kepler (Fig. 14-15; top row).

In summary, the thresholded power law seems to fit almost every data set, and thus does not justify additional free model parameters. The only two clear-cut deviations from a power law model are found for the cases of city sizes and forest fires, which may indeed reveal multiple scaling ranges, similar to multi-fractals in the geometric domain (Kelty-Stephen et al. 2013).

5.3. Differential Versus Cumulative Distributions

In this study we applied the thresholded power law model to both the differential and the cumulative size distribution functions. What do we learn from comparing these two methods? In principle we expect a higher accuracy for cumulative size distribution functions, because they always contain more datapoints per bin than the differential size distribution by definition. One difference is that the number of datapoints per bin is independent in the differential size distribution, while it is not for cumulative distributions. Nevertheless, our Monte-Carlo simulations have proven that a goodness-of-fit criterion can be defined for both methods (Eqs. 18-19), which both have a mean value of $\chi^2 \approx 1$ for random noise (although the value $\chi^2 \approx 0.8$ is slightly lower for cumulative distributions, see Fig. 5d). Applying both methods to the data, we find that the goodness-of-fit has the tendency to produce better fits for the cumulative size distributions than for the differential size distributions.

An important test is whether the two methods yield consistent values of power law slopes. We show the power law slope values $\alpha \pm \sigma_\alpha$ with errors in Fig. 16, which exhibits an excellent agreement between the differential (Fig. 16, x-axis) and the cumulative distribution values (Fig. 16, y=axis). Of course, the actual slope b of a cumulative distribution function is flatter by one, i.e., $b = a - 1$. The consistency of the two methods is largely obtained because both methods use the same threshold value x_0 and thus an identical subset of events for the fits. If the threshold x_0 is determined independently with the two methods, a discrepancy in the resulting power law slope values a would be unavoidable. In our study it was necessary to use both fitting procedures simultaneously, because the differential size distribution defines a more reliable threshold value x_0 (Fig. 6), while the cumulative size distribution appears to give better fits to the thresholded power law function (with a lower goodness-of-fit value χ^2).

5.4. Power laws and Physical Scaling Laws

Power laws are ubiquitous in statistical distributions of nonlinear energy dissipation events, a scientific research area that started with the model of self-organized criticality by Bak, Tang, and Wiesenfeld (1987). We outlined in Section 2.2 a basic derivation of a power law distribution that can be generated by any nonlinear process that produces exponentially growing avalanches and is stopped after a random time interval. Reed and Hughes (2002) describe a class of generative models for Pareto-type distributions that are multiplicative stochastic processes that are killed (i.e., stopped or observed) by a secondary process before equilibrium is established. An early application of this model is the acceleration of cosmic ray particles (Fermi 1949), while later applications considered accelerated particles, magnetic reconnection, and nonpotential energy build-up in solar flares as avalanching processes (Rosner and Vaiana 1978; Aschwanden et al. 1998; Lu and Hamilton 1991; Lu et al. 1993). Later applications included not only solar and stellar flares, but also auroral emission and geomagnetic substorms from planetary magnetospheres, particle events from radiation belts, pulsar glitches, soft gamma-ray repeaters, blazars, black-hole objects, cosmic rays, to boson clouds (for a recent review see Aschwanden et al. 2015 and references therein).

A discussion of power laws in all astrophysical applications is beyond the scope of this study, but we just want to point out the most fundamental reason why power laws are related to physical scaling laws. A mathematical derivation of power law size distributions for various observable parameters has been given in terms of the fractal-diffusive self-organized criticality (FD-SOC) model (Aschwanden 2012, 2015). The fundamental tenet of the FD-SOC model is the *scale-free probability conjecture*, which quantifies the statistical likelihood of avalanche sizes L with a reciprocal relationship to the volumes,

$$N(L)dL \propto L^{-d}dL \quad \text{for } L \leq L_{max} , \quad (22)$$

where d is the Euclidean dimension and L_{max} is the maximum avalanche size or finite system size. Geometric relationships, such as for the (avalanche) volume, $V \propto L^d$, predict then a power law for the size distribution of volumes V ,

$$N(V)dV \propto N(L[V]) \left| \frac{dL}{dV} \right| dV \propto V^{-(2-1/d)} dV \propto V^{-\alpha_V} dV . \quad (23)$$

Thus, in 3D space ($d = 3$), we expect that the avalanche volumes exhibit a size distribution of $N(V) \propto V^{5/3}$, with a power law index $\alpha_V \approx 1.67$. If there is a nonlinear scaling between the avalanche volume V and an observable, such as the energy E , which we quantify with the power index γ ,

$$E \propto V^\gamma , \quad (24)$$

we expect then a power law distribution $N(E)$ of

$$N(E)dE \propto N(V[E]) \left| \frac{dV}{dE} \right| dE \propto E^{-(1-1/d)/\gamma} dE \propto E^{-\alpha_E} dE . \quad (25)$$

Based on this scaling of the power law index $\alpha_E = 1 + (1 - 1/d)/\gamma$ we can then directly evaluate the nonlinear scaling index γ from a measurement of the power law slope α_E ,

$$\gamma = \frac{(1 - 1/d)}{(1 - \alpha_E)} . \quad (26)$$

This analytical derivation of power law distributions is entirely based on statistical probabilities and observables that are connected with geometric parameters by some power index. This explains the ubiquity of

power laws for the observables, but it does not explain the physics of the underlying process. The physics comes in with the scaling law between the observable and a geometric scale, i.e., $E \propto V^\gamma$. For a discussion of physical scaling laws applied to observed astrophysical processes see a recent review (e.g., Aschwanden et al. 2015).

The introduction of a threshold value x_0 into a pure power law function does not change the basic SOC concept, although it changes the value of the power law slope at the lower and upper boundary of an observed size distribution. Inclusion of this threshold value in fitting, however, allows us to evaluate a more accurate value of the underlying power law slope α , such as the observed slope α_E for energy size distributions (Eq. 25), and is therefore crucial for the identification or interpretation of the underlying physical scaling law. Since we have proven in this work that we can measure power law indices of observed size distributions down to an accuracy of $\lesssim 1\%$, we may refute the claim of Stumpf and Porter (2012) that the data are insufficient for the identification of power law behavior to be scientifically useful.

6. SUMMARY AND CONCLUSIONS

The fitting of ideal power law functions to real-world data is often hampered by two major problems, the problem of insufficient statistics (for extreme and rare events), and the problem of defining the correct size range where a power law fit is applied. Deviations from ideal power laws have been noted at the lower end, where often a smooth rollover occurs due to incomplete sampling at the sensitivity limit, and at the upper end, where a steepening in the cumulative size distribution occurs due to the cutoff of the largest event.

In this study we modify the ideal power law function by adding a constant x_0 , which has a three-fold meaning; (1) as a physical threshold of an instability (or exponentially growing avalanche process); and (2) as a sensitivity threshold for complete sampling; and (3) as a correction term for data samples that are contaminated by event-unrelated background noise. In addition we define an upper bound x_2 by the largest event, which represents a sharp cutoff in the differential size distribution and causes a gradual steepening at the upper end of the cumulative size distribution. With the introduction of these modifications we can fit most of the observed size distributions, as we tested with 9 mostly terrestrial data sets, 9 solar flare data sets (from the HXRBS, BATSE, RHESSI missions), and 9 stellar flare data sets (from the Kepler mission). We like to point out that the “thresholded power law model” used here is motivated by physical arguments (instability threshold, detection threshold, background noise), while alternative mathematical functions, such as power laws with an exponential cutoff, exponential functions, stretched exponentials, or log-normal functions, which all have been used in fitting of empirical data (Clauset et al. 2009), may have been chosen for mathematical convenience, rather than based on a specific physical model.

Our recommended procedure to fit power laws in data sets consists of the following four steps: (1) Histogram binning of both the differential and cumulative size distributions over the entire data range $[x_1, x_2]$; (2) Determination of a threshold x_0 from the bin with the maximum number of events in the differential size distribution; (3) Elimination of event-unrelated background b_0 by adjusting broken power laws to a straight power law in the fitting range $[x_0, x_2]$; and (4) Least-square fit by varying the power law slope a and normalization constant n_0 in the fitting range $[x_0, x_2]$, with evaluation of the goodness-of-fit criterion that reveals whether the thresholded power law model is consistent with the data or not.

The practical value of our thresholded power law model is reflected in a number of applications. Extreme events of solar flares, space weather storms, earthquakes, forest fires, blackouts, and terrorism are of high

interest for forecasting and mitigation of human risks and damage of electronic assets. Statistics of extreme events of stellar flares, cosmic rays, pulsar glitches, and gamma-ray bursts allow us to test physical models operating under most violent conditions in astrophysical particle accelerators and high-temperature plasmas. Measuring the power law slopes of multiple observables in an avalanching system, possibly governed by self-organized criticality, reveal us the degree of consistency with different models of physical scaling laws. The evaluation of threshold values is important for understanding the onset of instabilities and their triggers. In summary, there is a large number of applications in complexity theory and self-organized criticality models that benefit from reliable measurements of power law indices.

The author acknowledges the hospitality and partial support for two workshops on “Self-Organized Criticality and Turbulence” at the *International Space Science Institute (ISSI)* at Bern, Switzerland, during October 15-19, 2012, and September 16-20, 2013, as well as constructive and stimulating discussions with Sandra Chapman, Paul Charbonneau, Aaron Clauset, Michaila Dimitropoulou, Manolis Georgoulis, Stefan Hergarten, Henrik Jeldtoft Jensen, James McAteer, Shin Mineshige, Laura Morales, Mark Newman, Naoto Nishizuka, Gunnar Pruessner, John Rundle, Surja Sharma, Antoine Strugarek, Vadim Uritsky, and Nick Watkins. We thank also the anonymous statistical expert who provided links to the statistical literature, and the anonymous referee for thoughtful comments. This work was partially supported by NASA contract NNX11A099G “Self-organized criticality in solar physics” and NASA contract NNG04EA00C of the SDO/AIA instrument to LMSAL.

References

- Arnold, B.C. 2015 (2nd edition), 1983 (1st edition), “*Pareto Distributions*”, International Co-operative Publishing House. ISBN 0-89974-012-X.
- Aschwanden, M.J., Dennis, B.R., and Benz, A.O. 1998, *ApJ* 497, 972.
- Aschwanden, M.J. 2004, *Physics of the Solar Corona - An Introduction* (1st Edition), Praxis Publishing Ltd., Chichester UK, and Springer, New York, ISBN 3-540-22321-5, (842pp).
- Aschwanden, M.J. 2011a, *Solar Phys.* 274, 99.
- Aschwanden, M.J. 2011b, *SP* 274, 119.
- Aschwanden, M.J. 2011c, *Self-Organized Criticality in Astrophysics. The Statistics of Nonlinear Processes in the Universe*, Springer and PraXis: Berlin.
- Aschwanden, M.J. 2012, *AA* 539, A2 (15 p).
- Aschwanden, M.J., Crosby, N., Dimitropoulou, M., Georgoulis, M.K., Hergarten, S., McAteer, J., Milovanov, A., Mineshige, S., Morales, L., Nishizuka, N., Pruessner, G., Sanchez, R., Sharma, S., Strugarek, A., and Uritsky, V. 2015, *Space Science Reviews* (published online first), DOI 10.1007/s11214-014-0054-6, *25 Years of Self-Organized Criticality: Solar and Astrophysics*
- Bak, P., Tang, C., and Wiesenfeld, K. 1987, *PhRvL* 69/4, 381.
- Balona, L.A. 2015, *MNRAS* 447, 2714.
- Bauke, H. (2007), *Eur. Phys. J. B*, 58, 167.
- Baumjohann, W. and Treumann, R.A. 1996, *Basic space plasma physics*, Imperial College Press, London.
- Begelman, M.C., Volonteri, M., and Rees, M.J. 2006, *MNRAS* 370, 289.
- Bellán, P.M. 2006, *Fundamentals of plasma physics*, Cambridge University Press, Cambridge.
- Benz, A.O. 1993, *Plasma astrophysics, kinetic processes in solar and stellar coronae*, Kluwer Academic Publishers, Dordrecht, The Netherlands.
- Biesecker, D.A., Ryan, J.M., Fishman, G.J. 1993, *Lecture Notes in Physics* 432, 225.
- Biesecker, D.A. 1994, *On the occurrence of solar flares observed with the Burst and Transient Source Experiment (BATSE)*, PhD Thesis, University of New Hampshire.
- Biskamp, D. 2000, *Magnetic reconnection in plasmas*, Cambridge: Cambridge University Press.
- Boss, A.P. 1997, *Science* 276,(5320), 1836.
- Broder, A., Kumar, R., Maghoul, F., Raghavan, P., Rajagopalan, S., Stata, R., Tomkins, A., and Wiener, J., 2000, *Computer Networks* 33, 309.
- Bromund, K.R., McTiernan, J.M., Kane, S.R. 1995, *ApJ* 455, 733.
- Christe, S., Hannah, I.G., Krucker, S., McTiernan, J., and Lin, R.P. 2008, *ApJ* 677, 1385.
- Clauset, A., Young, M., and Gleditsch, K.S. 2007, *J. Conflict Resolution*, 51, 58.
- Clauset, A., Shalizi, C.R., and Newman, M.E.J. 2009, *SIAM Rev.* 51/4, 661.

- Cowling, T.G. 1976, *Magnetohydrodynamics*, Monographs on Astronomical Subjects 2, Adam Hilger Ltd., Bristol.
- Crosby, N.B., Aschwanden, M.J., and Dennis, B.R. 1993, *Solar Phys.* 143, 275.
- Crosby, N.B. 1996, *Contribution à l'Etude des Phénomènes Eruptifs du Soleil en Rayons à partir des Observations de l'Expérience WATCH sur le Satellite GRANAT*, PhD Thesis, Université Paris VII, Meudon, Paris.
- D'Agostino, R.B., and Stephens, M.A. (eds.), 1986, *Goodness-of-fit Techniques*, Marcel Dekker, New York.
- Datlowe, D.W., Elcan, M.J., and Hudson, H.S. 1974, *Solar Phys.* 39, 155.
- Dennis, B.R. 1985, *SP* 100, 465.
- Feigenbaum, J. 2003, *Rep. Prog. Phys.* 66, 1611.
- Fermi, E. 1949, *Phys. Rev. Lett.* 75, 1169.
- Georgoulis, M.K., Vilmer, N., and Crosby, N.B. 2001, *AA* 367, 326.
- Galam, S. 2012, *Sociophysics. A physicist's modeling of psycho-political phenomena*, Springer: New York.
- Giles, D.E., Feng, H., and Godwin, R. 2011, *Econometrics Working Paper EWP1104*, ISSN 1485-6441.
- Goldstein, M.L., Morris, S.A., and Yen, G.G. 2004, *Eur. Phys. J. B*, 41, 255.
- Goossens, M. 2003, *ApSS Library Vol. 294*, Dordrecht: Kluwer Academic Publishers, (405pp).
- Hosking, J.R.M. and Wallis, J.R. 1987, *Technometrics* 29(3), 339.
- Huberman, B.A. and Adamic, L. 1999, *Nature* 401, 131.
- Johnson, N.L., Kotz, S., Balakrishnan, N. 1994, *Continuous univariate distributions*, Vol. 1, Wiley Series in Probability and Statistics.
- Katz, J. 1986, *JGR* 91, 10412.
- Kelty-Stephen, D.G., Palatinus, K., Saltzman, E., and Dixon, J.A. 2013, *Ecological Psychology* 25, 1.
- Kivelson, M.G. and Russell, C.T. 1995, *Introduction to space physics*, Cambridge University Press, Cambridge, 568p.
- Koch, D.G., Borucki, W.J., Basrie, G., et al. 2010, *ApJ* 713, 79.
- Krall, K.R. and Trivelpiece 1971, *Principles of Plasma Physics*, McGraw-Hill Book Company.
- Lee, T.T., Petrosian, V., and McTiernan, J.M. 1993, *ApJ* 412, 401.
- Lin, R.P., Schwartz, R.A., Kane, S.R., Pelling, R.M., Hurley, K.C. 1984, *ApJ* 283, 421.
- Lin, R.P., Feffer, P.T., and Schwartz, R.A. 2001, *ApJ* 557, L125.
- Lomax, K.S. 1954, *J. American Statistical Association* 49, 847.
- Lu, E.T. and Hamilton, R.J., 1991, *ApJ* 380, L89.
- Lu, E.T., Hamilton, R.J., McTiernan, J.M., and Bromund, K.R. 1993, *ApJ* 412, 841.
- Lui, A.T.Y. 1991, *JGR* 96, 1849.

- Maehara, H., Shibayama, T., Notsu, S. et al. 2012, *Nature* 485, 478.
- Mandelbrot, B.B. 1977, *Fractals: form, chance, and dimension*, Translation of *Les objets fractals*, W.H. Freeman, San Francisco.
- Melrose, D.B. 1980a, *Plasma Astrophysics. Nonthermal Processes in Diffuse Magnetized Plasmas. Volume 1: The Emission, Absorption and Transfer of Waves in Plasmas*, Gordon and Breach Science Publishers, New York.
- Melrose, D.B. 1980b, *Plasma Astrophysics. Nonthermal Processes in Diffuse Magnetized Plasmas. Volume 2: Astrophysical Applications*, Gordon and Breach Science Publishers, New York.
- Melrose, D.B. 1986, *Instabilities in space and laboratory plasmas*, Cambridge University Press, Cambridge.
- Newman, M.E.J. 2005, *Contemporary Physics* 46, 323.
- Perez Enriquez, R., Miroshnichenko, L.I. 1999, *Sol. Phys.* 188, 169.
- Press, W.H., Flannery, B.P., Teukolsky, S.A., and Vetterling, W.T. 1986, *Numerical recipes, The Art of Scientific Computing*, Cambridge.
- Priest, E.R. 1982, *Solar Magnetohydrodynamics*, Geophysics and Astrophysics Monographs, Vol. 21, D.Reidel Publishing Company, Dordrecht.
- Priest, E.R. and Forbes, T. 2000, *Magnetic reconnection (MHD Theory and Applications)*, Cambridge: Cambridge University Press.
- Priest, E.R. 1978, *Solar Phys.* 58, 57.
- Pruessner, G. 2012, *Self-organised criticality. Theory, models and characterisation*, Cambridge University Press.
- Reed, W.J. and Hughes, B.D. 2002, *Phys. Rev. Lett.* E 66, 067103.
- Rosner, R. and Vaiana, G.S. 1978 *ApJ* 222, 1104.
- Schmidt, G. 1979, *Physics of high temperature plasmas*, (2nd edition), Academic Press, New York.
- Schwartz, R.A., Dennis, B.R., Fishman, G.J., Meegan, C.A., Wilson, R.B., Paciesas, W.S. 1992, in Shrader, C.R., Gehrels, N., Dennis, B.R. (eds.), *The Compton Observatory Science Workshop*, NASA CP **3137**, NASA: Washington DC, 457.
- Shibayama, T., Maehara, H., Notsu, S. et al. 2013, *ApJSS* 209, 5.
- Shibaskai, K. 2001, *ApJ* 557, 326.
- Smith, R.A., Goldstein, M.L., and Papadopoulos, K. 1979, *ApJ* 234, 348.
- Somov, B.V. 2000, *Cosmic plasma physics*, ApSS Library, Vol. 251, (672pp.), Kluwer Academic Publishers, Dordrecht.
- Springel, V., White, S.D.M., Jenkins, A., et al. 2005, *Nature* 435, 629.
- Stumpf, M.P.H. and Porter, M.A. 2012, *Science* 335, issue 10 Feb 2012.
- Sturrock, P.A. 1994, *Plasma physics. An introduction to the theory of astrophysica, geophysical and laboratory plasmas*, Cambridge University Press, Cambridge.

- Su, Y., Gan, W.Q., and Li, Y.P. 2006, *Solar Phys.* 238, 61.
- Tajima, T. and Shibata, K. 2002, *Plasma astrophysics*, Perseus Publishing, Cambridge, Massachusetts.
- Tranquille, C., Hurley, K., and Hudson, H.S. 2009, *Solar Phys.* 258, 141.
- Treumann, R.A. and Baumjohann, W. 1997, *Advanced space plasma physics*, Imperial College London.
- Turcotte, D.L. 1999, *Phys. Earth Planet Inter.* 111, 275.
- Walkowicz, L.M., Basri, G., Batalha, N. et al. 2011, *ApJ* 141, 50.
- Wang, B. and Silk, J. 1994, *ApJ* 427, 759.
- Willis, J.C. and Yule, G.U. 1922, *Nature* 109, 177.
- Wu, C.J., Ip, W.H., and Huang, L.C. 2015, *ApJ* 798, 92.
- Wu, C.S. and Lee, L.C. 1979, *ApJ* 230, 621.

Table 1: A selection of hydrodynamic, magneto-hydrodynamic, and kinetic instabilities and threshold conditions, occurring in solar and astrophysical plasmas.

Instability	Threshold condition
Interchange or Pressure-Driven Instabilities:	
<i>Rayleigh–Taylor instability:</i>	
Hydrodynamic	$\mathbf{g} \cdot \nabla n_0 < 0$
Hydromagnetic (Kruskal–Schwarzschild)	$\mathbf{k} \cdot \mathbf{B} = 0$
Hydromagnetic (Parker instability)	$\mathbf{k} \cdot \mathbf{B} \neq 0$
<i>Kelvin–Helmholtz instability</i>	
Hydromagnetic:	$v_1 > v_{A,2}$
<i>Ballooning instability</i>	$\mathbf{j} \times \mathbf{B} > \rho \mathbf{g}$
Thermal Instabilities:	
<i>Convective instabilities</i>	$(dT/dz)_{crit}$
<i>Radiatively-driven thermal instabilities</i>	$\tau_{cond} > \tau_{rad}$
<i>Heating-driven thermal instabilities</i>	$s_H/L < 1/3$
Resistive Instabilities:	
<i>Gravitational mode</i>	$F_{grav} > (\mathbf{j} \times \mathbf{B})$
<i>Rippling mode</i>	$F_{adv} > (\mathbf{j} \times \mathbf{B})$
<i>Tearing mode</i>	$(dB/dx)_{crit}$
Current Pinch Instabilities:	
<i>Cylindrical pinch:</i>	
Kink mode	$B_{0\varphi}^2 \ln(L/a) > B_{0z}^2$
Sausage mode	$B_{0\varphi}^2 > 2B_{0z}^2$
Helical/torsional mode	$B_{0\varphi} > (2\pi a/L)B_{0z}$
<i>Current sheet:</i>	
Kinetic Instabilities:	
<i>Bump-in-tail instability</i>	$df(v_{\parallel})/dv_{\parallel} \gtrsim 0$
<i>Loss-cone instability</i>	$df(v_{\perp})/dv_{\perp} \gtrsim 0$
<i>Buneman instability</i>	$v_d \gtrsim 1.7(v_{te} + v_{ti})$

Table 2: Power law slopes of (terrestrial and empirical) data (Clauset et al. 2009).

Dataset	Number	Threshold	Back- ground	Differential slope	Cumulative slope	Clauset slope	Differential fit	Cumulative fit
		x_0	b_0	a_{diff}	a_{cum}	a	χ^2	χ^2
(a) Flares	12772	15.8	57	1.72 ± 0.02	1.72 ± 0.02	1.79 ± 0.02	0.9	0.6
(b) Quakes	19301	861	1	1.85 ± 0.02	1.84 ± 0.01	1.64 ± 0.04	2.5	1.3
(c) Fires	203784	0.63	1	1.42 ± 0.01	1.48 ± 0.01	2.20 ± 0.30	23.2	15.1
(d) Cities	19446	631	0	1.82 ± 0.02	1.85 ± 0.01	2.38 ± 0.08	5.2	7.2
(e) Blackouts	210	39800	0	1.84 ± 0.15	1.88 ± 0.13	2.30 ± 0.03	0.6	0.4
(f) Terrorism	9100	1	2	1.99 ± 0.04	2.00 ± 0.04	2.40 ± 0.02	4.0	2.7
(g) Words	18855	1	1	1.98 ± 0.02	1.92 ± 0.02	1.95 ± 0.02	7.0	3.2
(h) Surnames	19301	19700	2	2.74 ± 0.07	2.61 ± 0.06	2.50 ± 0.02	2.4	1.1
(i) Weblinks	$2.4 \cdot 10^8$	1	1	2.35 ± 0.00	2.13 ± 0.00	2.34 ± 0.01	1078	623

Table 3: Frequency distributions measured from solar flares in hard X-rays and γ -rays. The prediction is based on the FD-SOC model (Aschwanden 2012).

Power law slope of peak flux α_P	Power law slope of fluence α_E	Power law slope of durations α_T	Number of events n	Instrument and threshold energy	References
1.8			123	OSO-7(>20 keV)	¹⁾ Datlowe et al. (1974)
2.0			25	UCB(>20 keV)	²⁾ Lin et al. (1984)
1.8			6775	HXRBS(>20 keV)	³⁾ Dennis (1985)
1.73 \pm 0.01			12,500	HXRBS(>25 keV)	⁴⁾ Schwartz et al. (1992)
1.73 \pm 0.01	1.53 \pm 0.02	2.17 \pm 0.05	7045	HXRBS(>25 keV)	⁵⁾ Crosby et al. (1993)
1.71 \pm 0.04	1.51 \pm 0.04	1.95 \pm 0.09	1008	HXRBS(>25 keV)	⁶⁾ Crosby et al. (1993)
1.68 \pm 0.07	1.48 \pm 0.02	2.22 \pm 0.13	545	HXRBS(>25 keV)	⁷⁾ Crosby et al. (1993)
1.67 \pm 0.03	1.53 \pm 0.02	1.99 \pm 0.06	3874	HXRBS(>25 keV)	⁸⁾ Crosby et al. (1993)
1.61 \pm 0.03			1263	BATSE(>25 keV)	⁹⁾ Schwartz et al. (1992)
1.75 \pm 0.02			2156	BATSE(>25 keV)	¹⁰⁾ Biesecker et al. (1993)
1.79 \pm 0.04			1358	BATSE(>25 keV)	¹¹⁾ Biesecker et al. (1994)
1.59 \pm 0.02		2.28 \pm 0.08	1546	WATCH(>10 keV)	¹²⁾ Crosby (1996)
1.86	1.51	1.88	4356	ISEE-3(>25 keV)	¹³⁾ Lu et al. (1993)
1.75	1.62	2.73	4356	ISEE-3(>25 keV)	¹⁴⁾ Lee et al. (1993)
1.86 \pm 0.01	1.74 \pm 0.04	2.40 \pm 0.04	3468	ISEE-3(>25 keV)	¹⁵⁾ Bromund et al. (1995)
1.80 \pm 0.01	1.39 \pm 0.01		110	PHEBUS(>100 keV)	¹⁶⁾ Perez-Enriquez & Miroshnichenko (1999)
1.80 \pm 0.02		2.2 \pm 1.4	2759	RHESSI(>12 keV)	¹⁷⁾ Su et al. (2006)
1.58 \pm 0.02	1.7 \pm 0.1	2.2 \pm 0.2	4241	RHESSI(>12 keV)	¹⁸⁾ Christe et al. (2008)
1.6			243	BATSE(>8 keV)	¹⁹⁾ Lin et al. (2001)
1.61 \pm 0.04			59	ULYSSES(>25 keV)	²⁰⁾ Tranquille et al. (2009)
1.74 \pm 0.02	1.66 \pm 0.02	2.54 \pm 0.02	10291	HXRBS(>25 keV)	²¹⁾ This work (cumulative)
1.75 \pm 0.02	1.69 \pm 0.03	2.57 \pm 0.03	10291	HXRBS(>25 keV)	²²⁾ This work (differential)
1.79 \pm 0.02	1.61 \pm 0.03	2.32 \pm 0.03	7233	BATSE(>25 keV)	²³⁾ This work (cumulative)
1.89 \pm 0.02	1.63 \pm 0.04	2.23 \pm 0.03	7233	BATSE(>25 keV)	²⁴⁾ This work (differential)
1.81 \pm 0.03	1.62 \pm 0.02	1.96 \pm 0.02	11549	RHESSI(>25 keV)	²⁵⁾ This work (cumulative)
1.82 \pm 0.04	1.58 \pm 0.02	1.95 \pm 0.02	11549	RHESSI(>25 keV)	²⁶⁾ This work (differential)
1.67	1.50	2.00		FD-SOC prediction	Aschwanden (2012)

Table 4: Frequency distributions of bolometric energies radiated in stellar flares observed with Kepler.

Star	Instrument	Number of events	Power law slope differential α_{dif}	power law slope cumulative α_{cum}	References:
G5-stars	Kepler	365	2.3±0.3		Maehara et al. (2012)
G5-stars slow	Kepler	101	2.0±0.2		Maehara et al. (2012)
G5-stars	Kepler	1547	2.2		Shibayama et al. (2013)
G5-stars slow	Kepler	397	2.0		Shibayama et al. (2013)
G5-stars	Kepler	1538	2.04±0.13		Aschwanden (2015)
G5-stars	Kepler	1538	2.43±0.08	2.42±0.06	This study
G-type stars	Kepler	4494	2.04±0.17		Wu et al. (2015)
K-M,A-F stars	Kepler	209	1.69±0.16	1.71±0.12	Balona (2015), This study
KID3557532	Kepler	196	2.11±0.19		Wu et al. (2015)
KID6034120	Kepler	45	3.12±0.60	3.17±0.48	This study
KID6697041	Kepler	37	1.83±0.37	1.51±0.25	This study
KID6865416	Kepler	147	1.77±0.10		Wu et al. (2015)
KID75264976	Kepler	40	1.92±0.34	1.98±0.32	This study
KID7532880	Kepler	159	1.90±0.16		Wu et al. (2015)
KID8074287	Kepler	160	1.87±0.10		Wu et al. (2015)
KID8479655	Kepler	39	1.45±0.23	1.47±0.24	This study
KID8547383	Kepler	40	3.41±0.68	2.58±0.41	This study
KID9653110	Kepler	158	1.64±0.07		Wu et al. (2015)
KID10422252	Kepler	177	1.75±0.08		Wu et al. (2015)
KID10422252	Kepler	57	2.99±0.58	2.78±0.37	This study
KID10745663	Kepler	137	1.63±0.10		Wu et al. (2015)
KID11551430	Kepler	202	1.59±0.06		Wu et al. (2015)

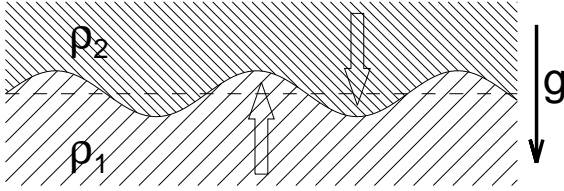
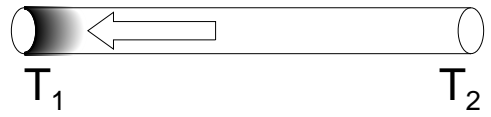
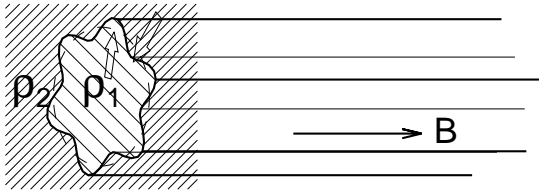
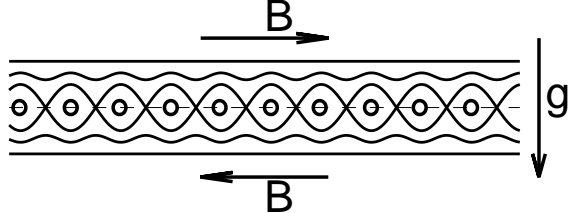
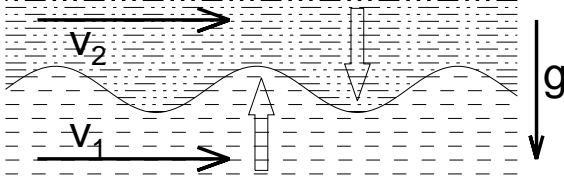
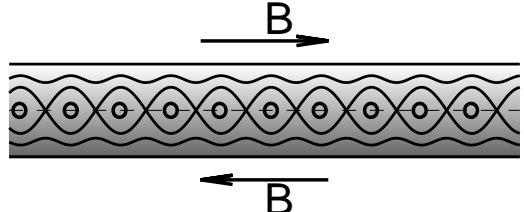
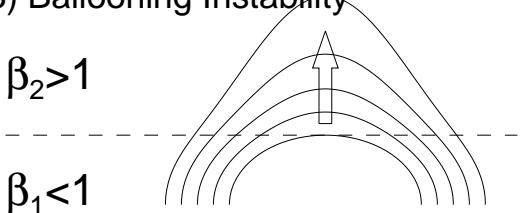
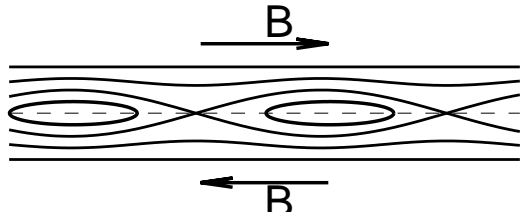
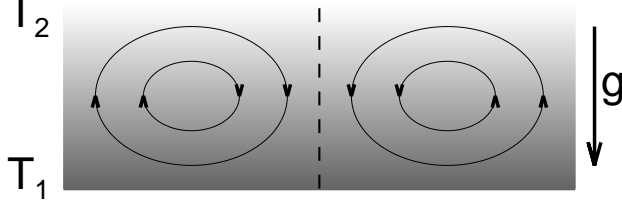
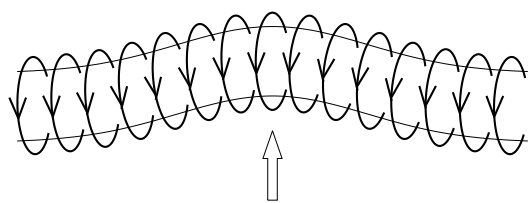
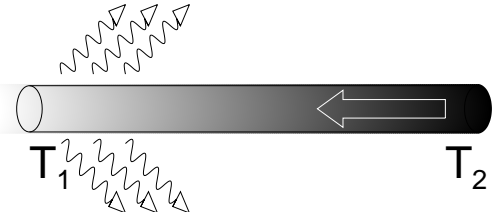
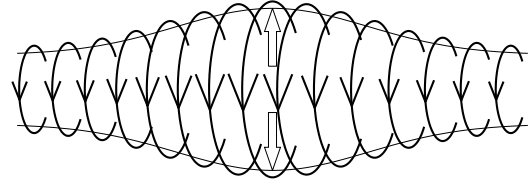
<p>1.1.1) Rayleigh-Taylor Instability</p> 	<p>2.3) Heating Scale-Height Instability</p> 
<p>1.1.2) Kruskal-Schwarzschild Instability</p> 	<p>3.1) Gravitational Mode Instability</p> 
<p>1.2) Kelvin-Helmholtz Instability</p> 	<p>3.2) Rippling Mode Instability</p> 
<p>1.3) Ballooning Instability</p> <p>$\beta_2 > 1$</p> <p>$\beta_1 < 1$</p> 	<p>3.3) Tearing Mode Instability</p> 
<p>2.1) Convective Instability</p> <p>T_2</p> <p>T_1</p> 	<p>4.1) Kink Instability</p> 
<p>2.2) Radiative Thermal Instability</p> <p>T_1</p> <p>T_2</p> 	<p>4.2) Sausage Instability</p> 

Fig. 1.— Hydrodynamic and magneto-hydrodynamic instabilities that can occur in astrophysical plasmas are illustrated (in the same order as in Table 1). Different densities (ρ_1, ρ_2) are rendered with hatched linestyle, different velocities (v_1, v_2) with dashed linestyle, temperature gradients (T_1, T_2) with greyscales, magnetic field lines (B) with thin solid lines, and gravity (g) with a vertical arrow pointing down.

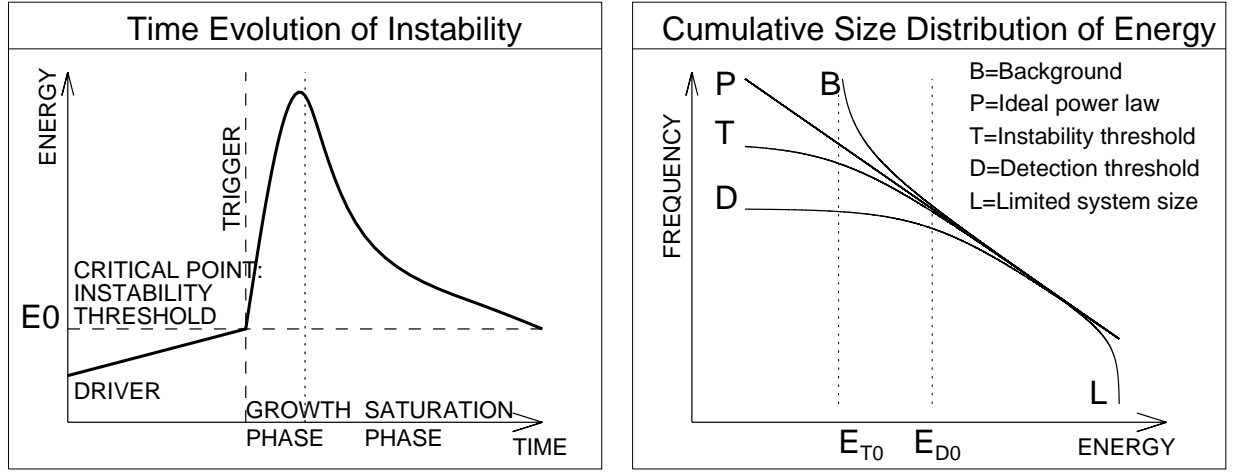


Fig. 2.— *Left*: Schematic time evolution of an instability, which has an onset when the energy parameter exceeds a critical point or instability threshold E_{T0} . *Right*: Deviations from an ideal power law (P) of the cumulative size distribution of energies occur when a background is present (B), when the sample contains values below the instability threshold E_{T0} (T), when the instrumental sensitivity sets a detection threshold E_{D0} (D), and when a (finite) limited system size is present (L).

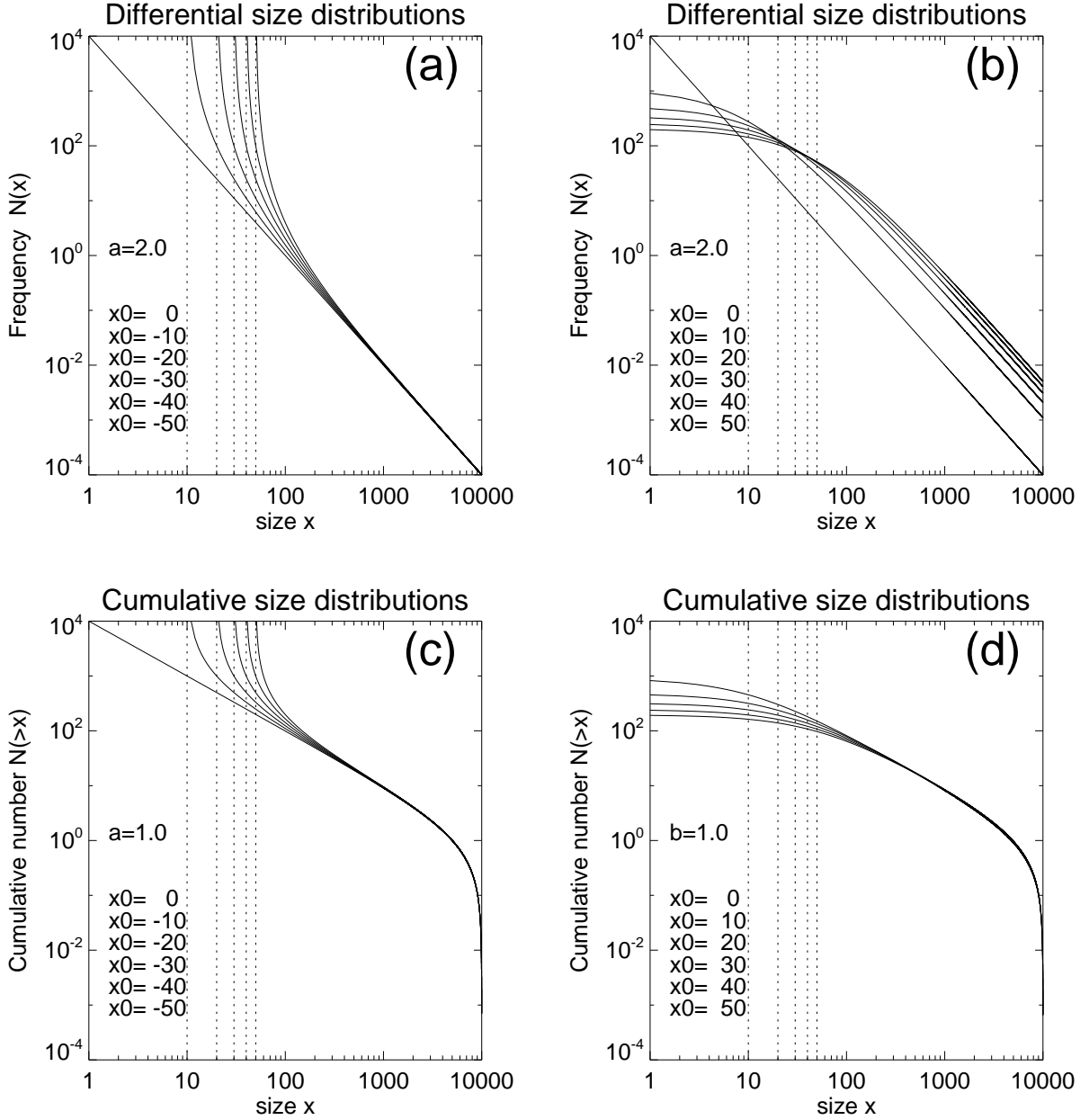


Fig. 3.— Differential (top) and cumulative occurrence frequency distributions (bottom) for a power law slope of $a = 2.0$ (or cumulative slopes $b = a - 1 = 1.0$) and a range of negative (left) and positive (right) threshold values x_0 . Note that the cumulative distributions show a steep drop-off at the maximum value near $x \lesssim 10^4$.

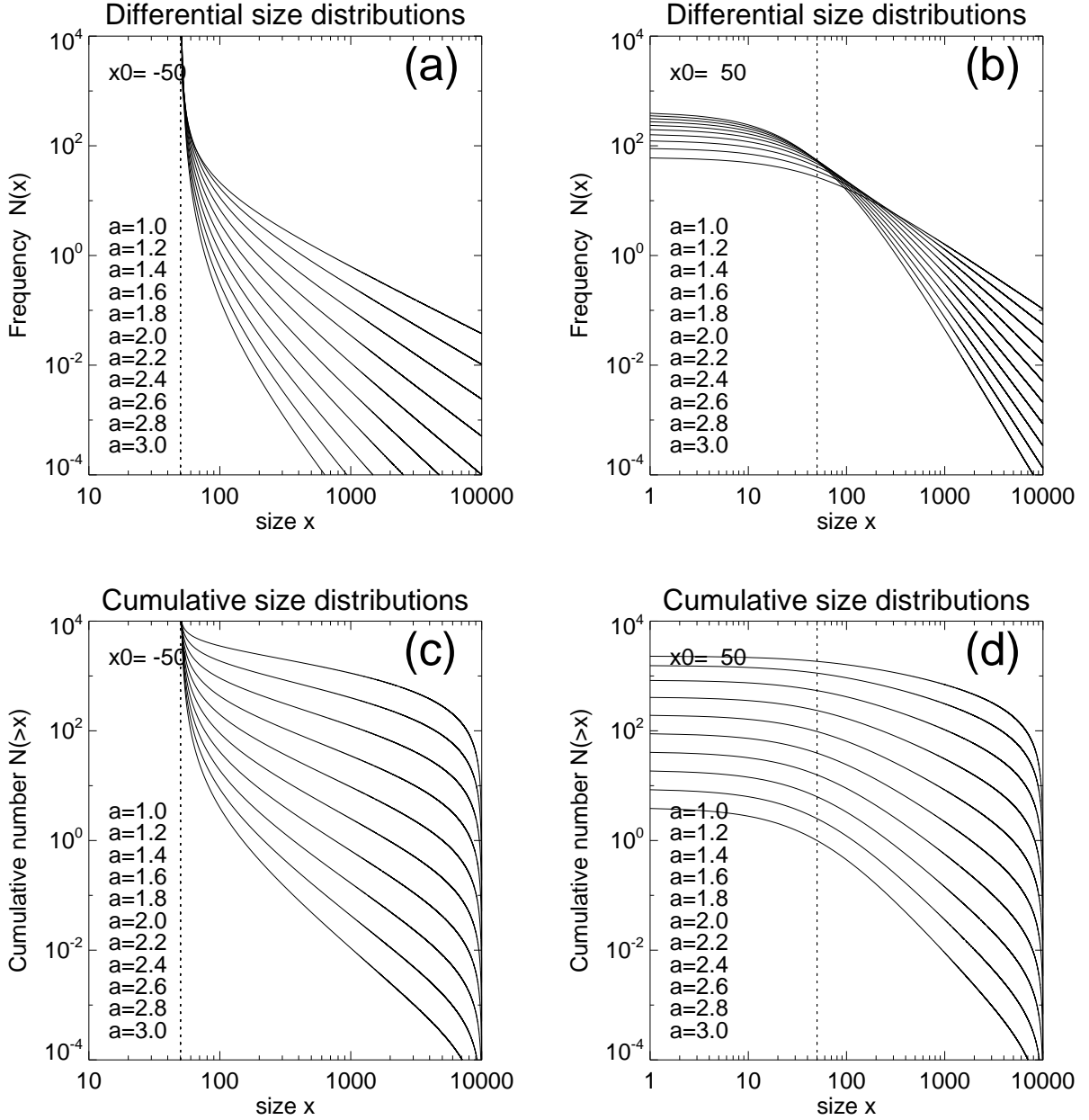


Fig. 4.— Differential (top) and cumulative occurrence frequency distributions (bottom) for a range of power law slopes of $a = 1.0, \dots, 3.0$ (or cumulative slopes $b = a - 1$), with a negative (left) or positive (right panels) threshold value x_0 . Note that the cumulative distributions show a steep drop-off at the maximum value near $x \lesssim 10^4$.

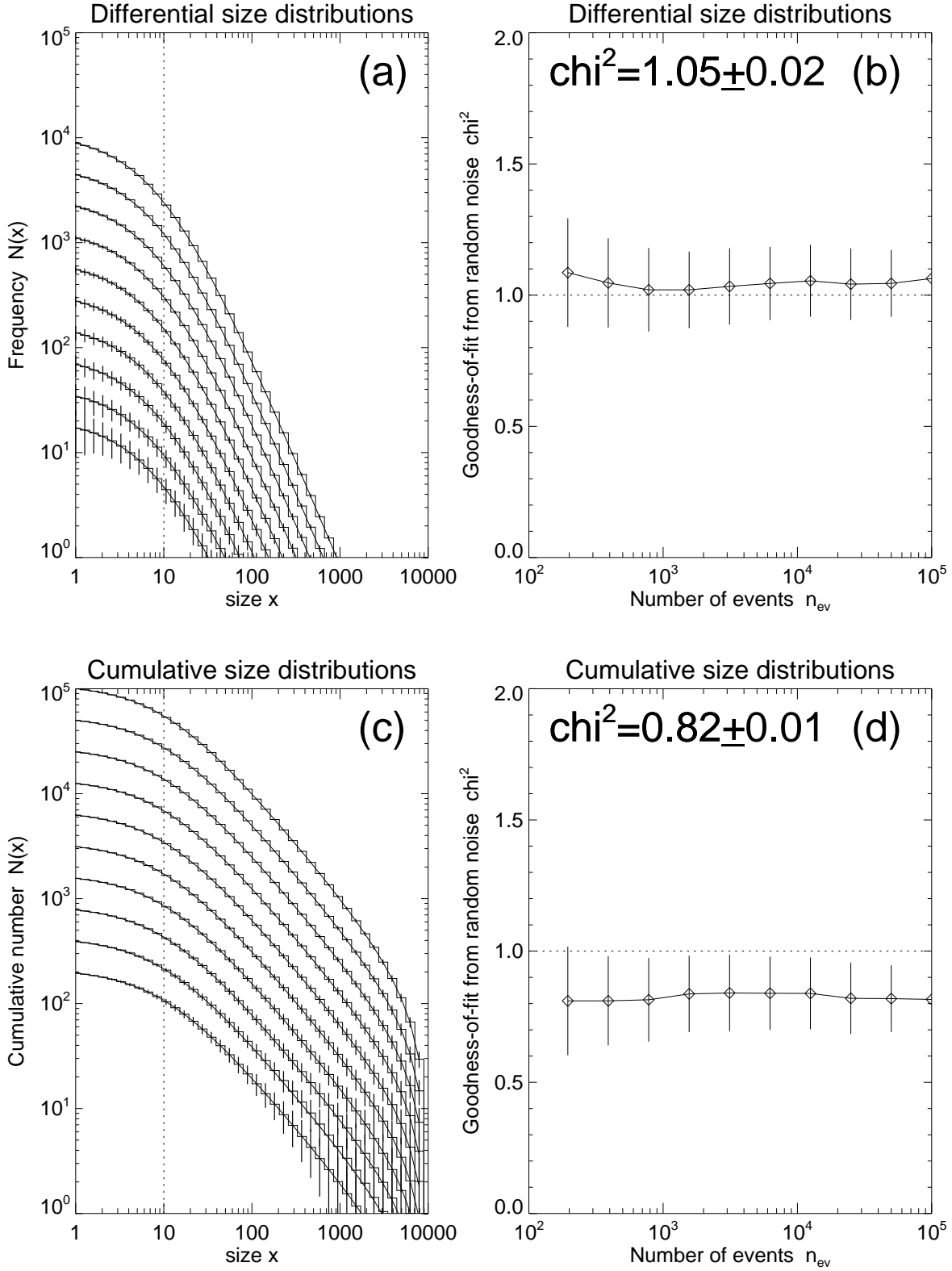


Fig. 5.— Numerical simulations of differential (top panels) and cumulative (bottom panels) size distributions for thresholded power law distributions with the parameters $x_0 = 10$, $a = 2.0$, $n_{ev} = 10^5, \dots, 195$, where the number of events decreases by a factor of two for each of the 10 data sets. The theoretical distribution function is plotted with a smooth curve, while the simulated data using a random generator are shown in form of histograms with error bars, each set showing the average and standard deviations **from 1000**

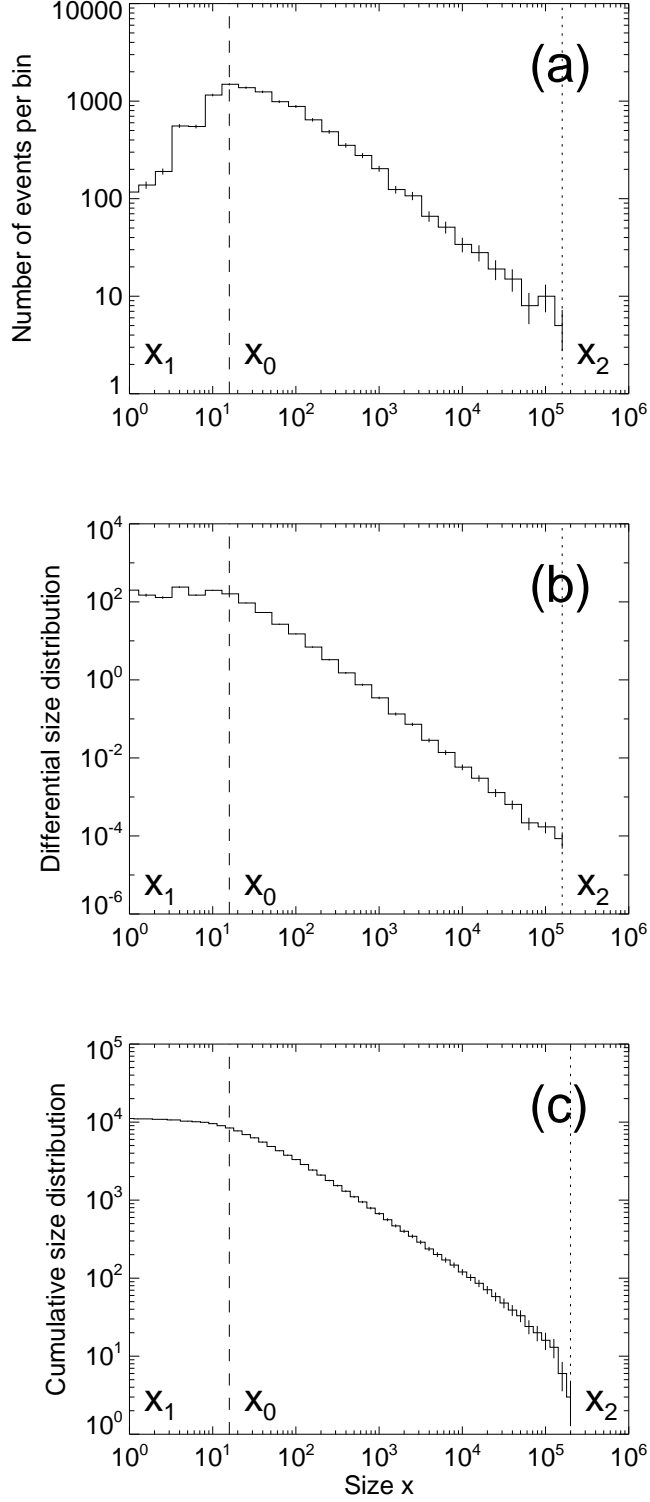


Fig. 6.— The determination of the lower threshold x_0 of a completely sampled power law distribution is obtained from the maximum in the distribution of sampled events per bin $N_{bin,i}$ (top panel), which generally coincides with a flat rollover at the lower end of the differential size distribution $N(x) = N_{bin,i}/\Delta x$ (middle panel), or in the cumulative size distribution $N_{cum}(> x)$ (bottom panel). The distributions shown here refer to a data set with 10,665 solar flare events described in Section 4.1.

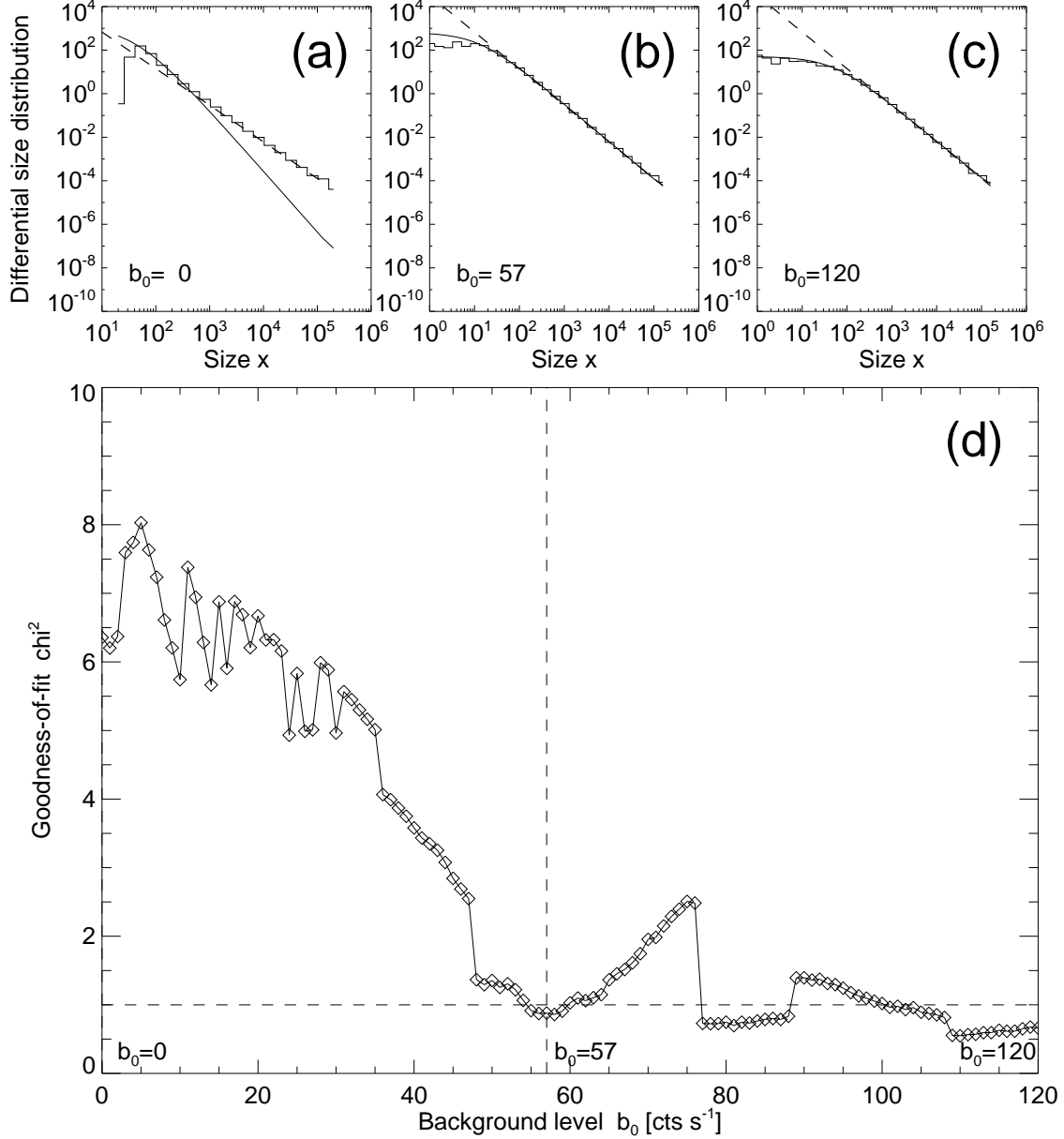


Fig. 7.— The background subtraction procedure is shown for the same solar flare data set as shown in Fig. 6. Three examples of differential size distributions sampled with different background subtractions of $b_0 = 0, 57, 120 \text{ cts s}^{-1}$ are shown (histograms in top panels), along with fits of thresholded power law distributions (smooth curves in top panels) and the power law slopes (dashed lines in top panels). The goodness-of-fit χ^2 is shown as a function of 120 different background levels ($b_0 = 1, 2, \dots, 120 \text{ cts s}^{-1}$) in the bottom panel. Note that a best-fit value of $\chi^2 \approx 1.0$ is obtained empirically for an optimum background value of $b_0 = 57 \text{ cts s}^{-1}$.

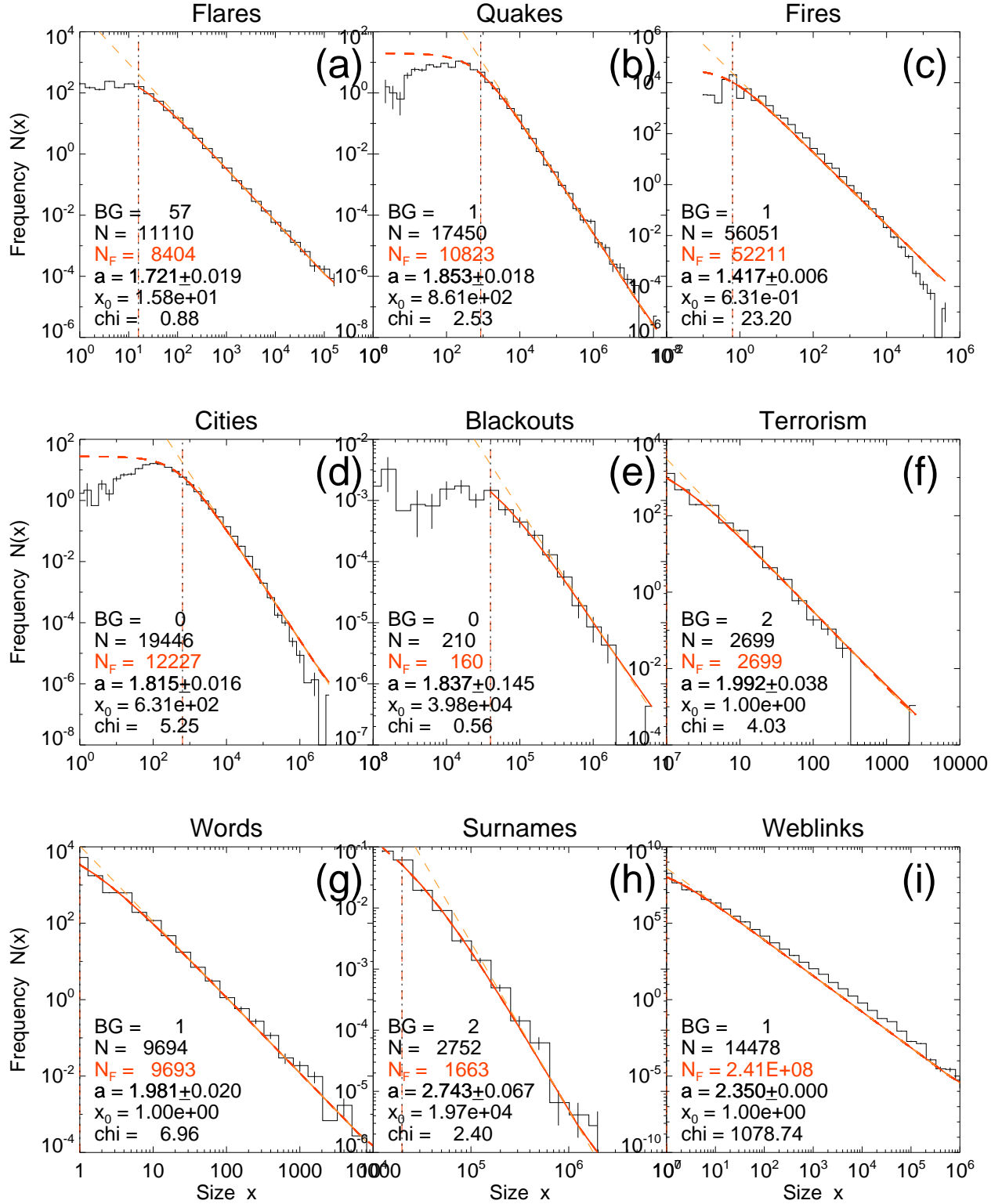


Fig. 8.— Differential size distributions (histogram) with fits (red curve) of thresholded power laws for 9 empirical data sets from Clauset et al. 2009. A straight power law is indicated with a dashed orange line. The threshold x_0 found from the fit is indicated with a vertical dotted line. The number of all events (N), of the partial events in the range of $x > x_0$, the power law slopes a , the backgrounds BG , the thresholds x_0 , and the goodness-of-fit χ^2 are listed also.

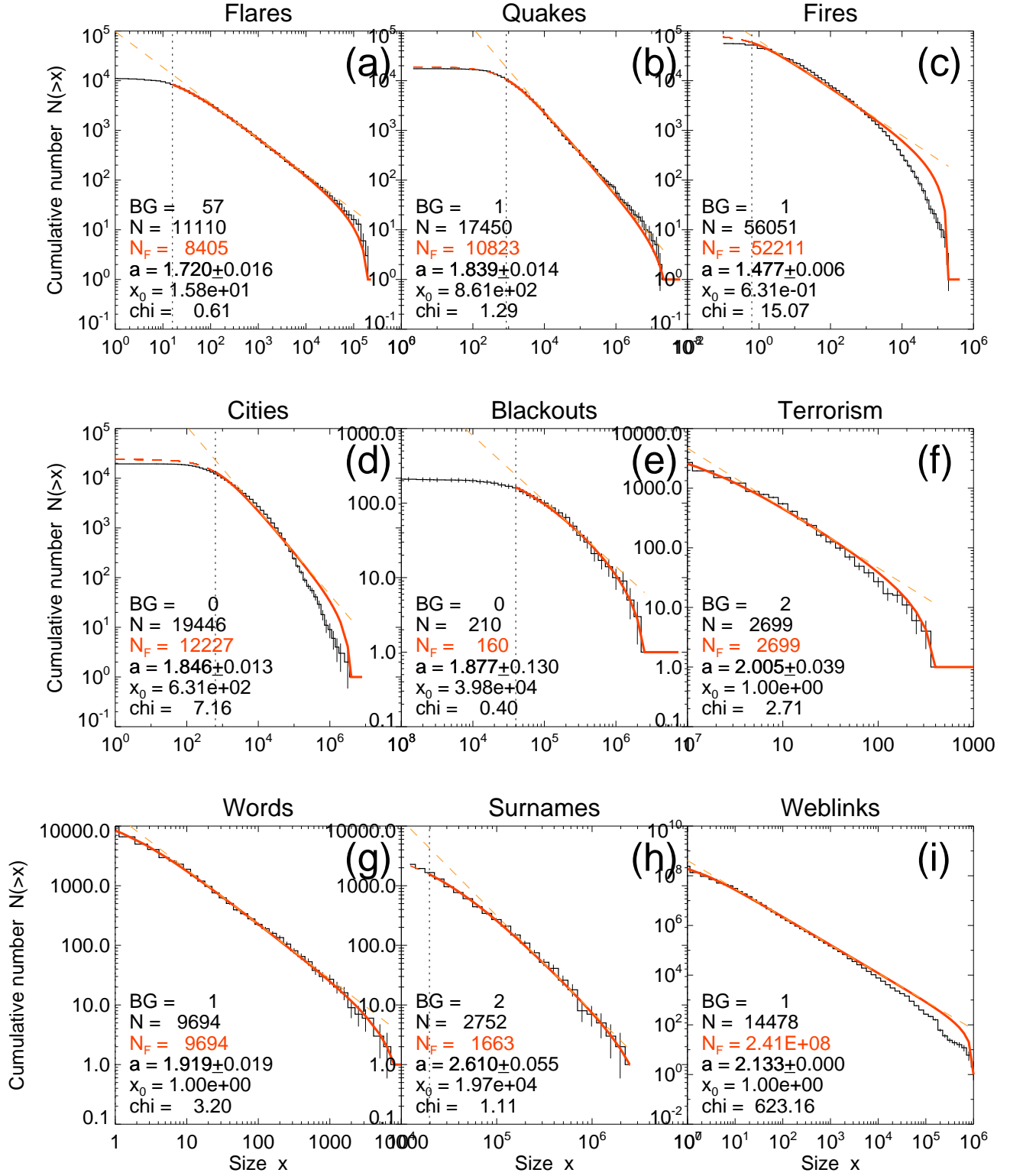


Fig. 9.— Cumulative size distributions (histogram) with fits (red curve) of thresholded power laws for 9 empirical data sets from Clauset et al. 2009. Representation similar to Figure 8.

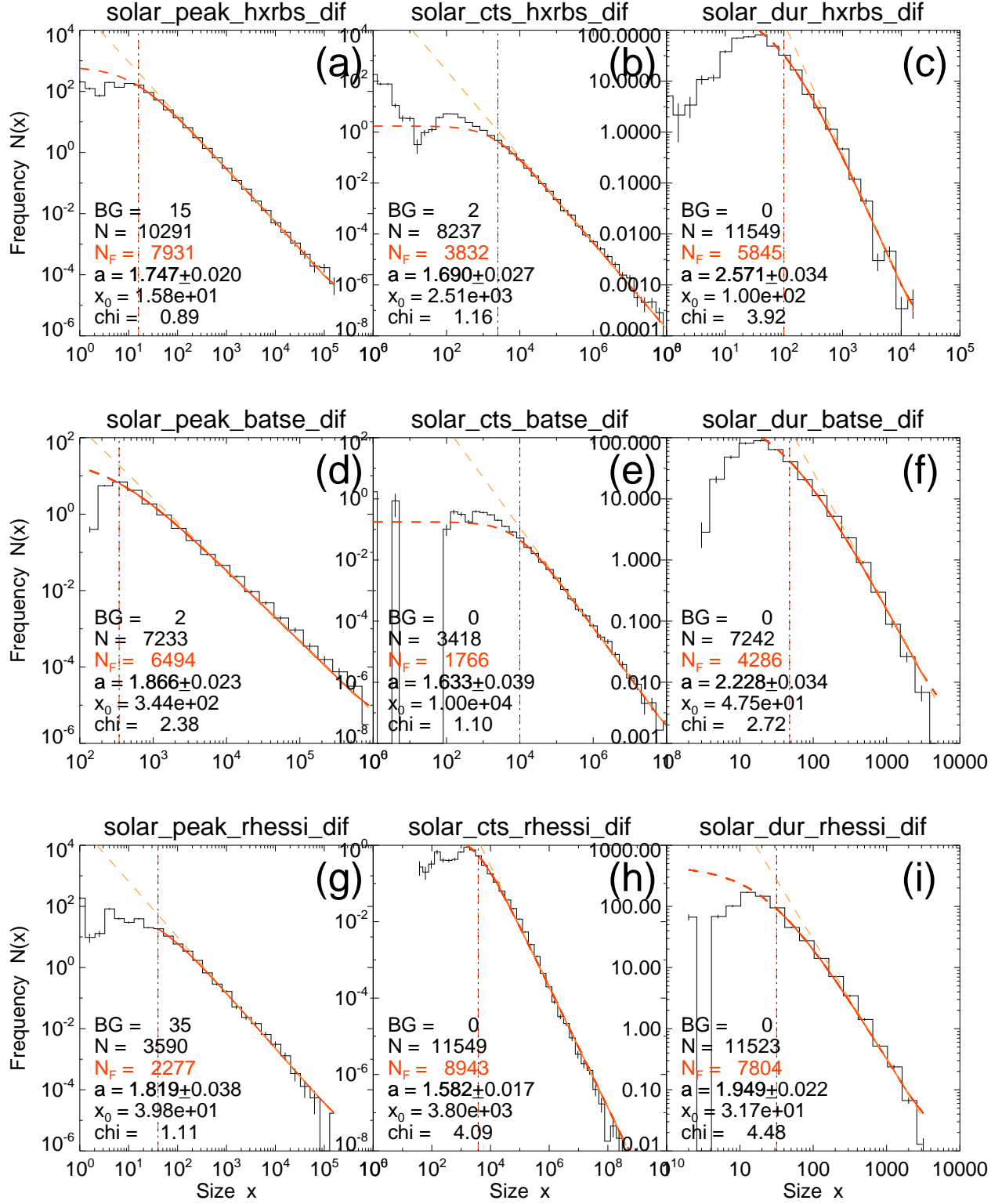


Fig. 10.— The differential size distributions of hard X-ray peak counts (left), total counts (middle), and durations of solar flare events (right panel), are shown from HXRBS/SMM (top row), BATSE/CGRO (middle row), and RHESSI data (bottom row).

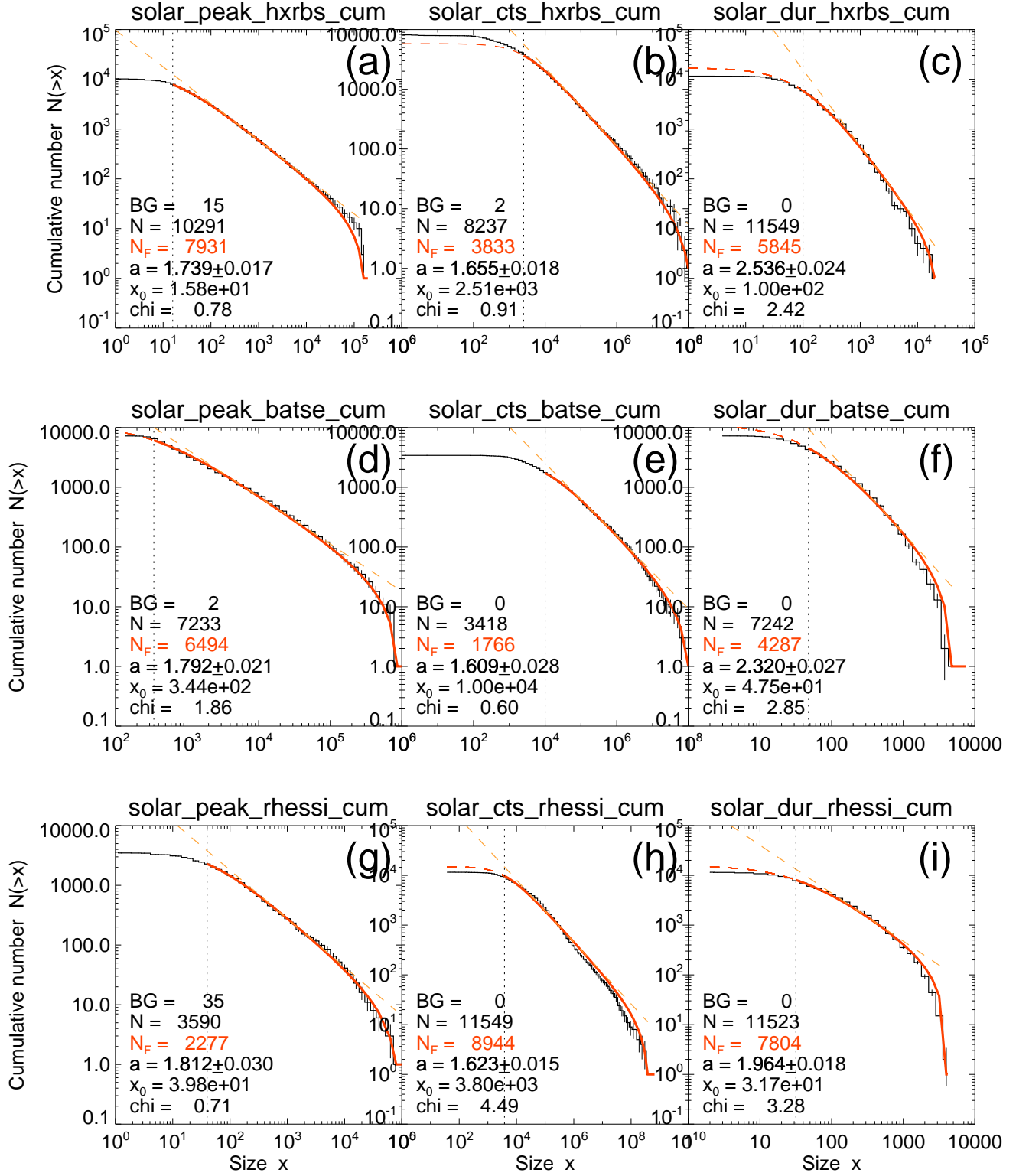


Fig. 11.— The cumulative size distributions of hard X-ray peak counts (left), total counts (middle), and durations of solar flare events (right panel), are shown from HXRBS/SMM (top row), BATSE/CGRO (middle row), and RHESSI data (bottom row). Representation similar to Fig. 10.

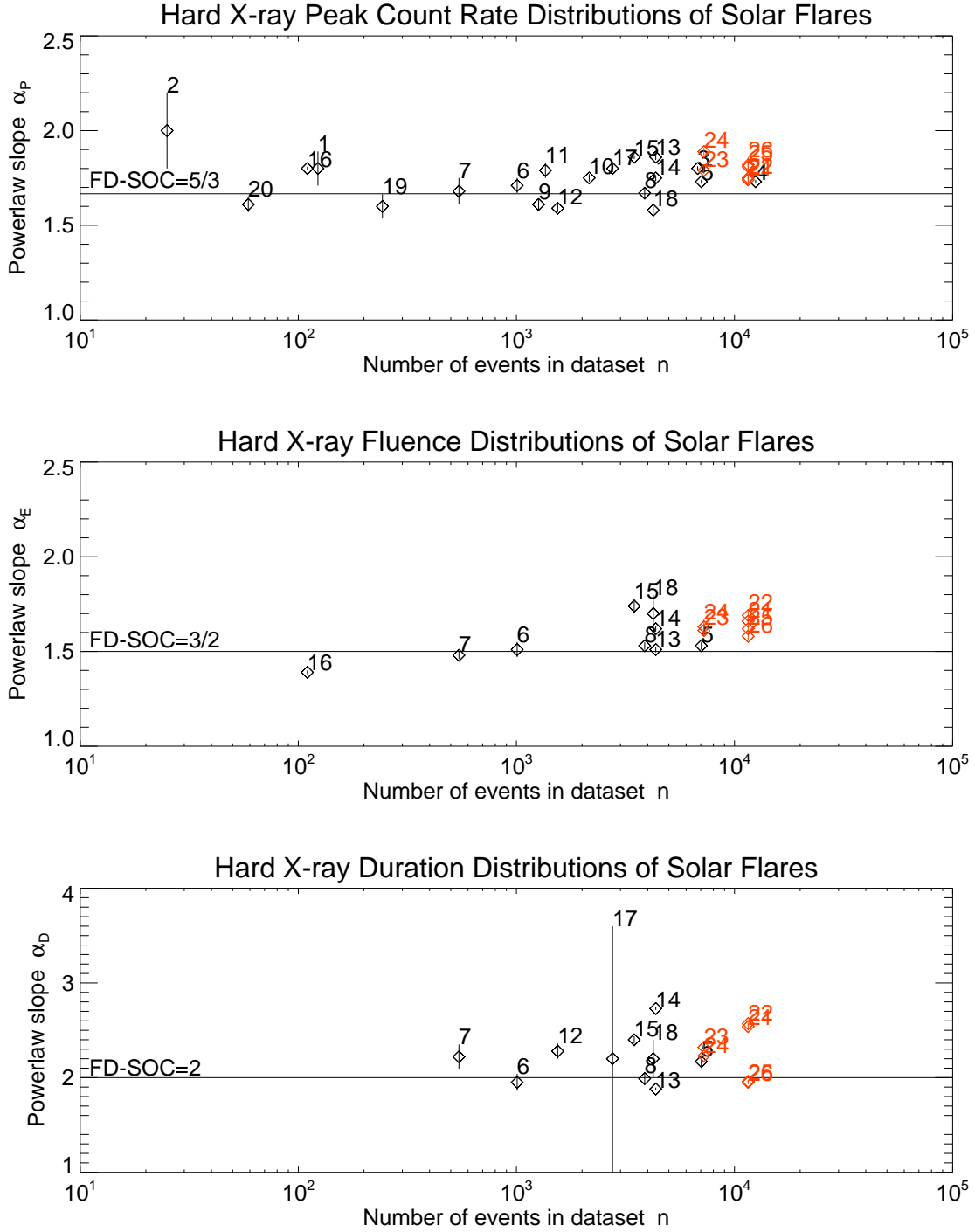


Fig. 12.— The power law slopes of hard X-ray peak counts (top), fluences (middle), and flare durations (bottom) are shown as a function of the number of events n in each data set published earlier (small diamonds) or analyzed in this study (red diamonds). The numbers refer to the references of Table 3.

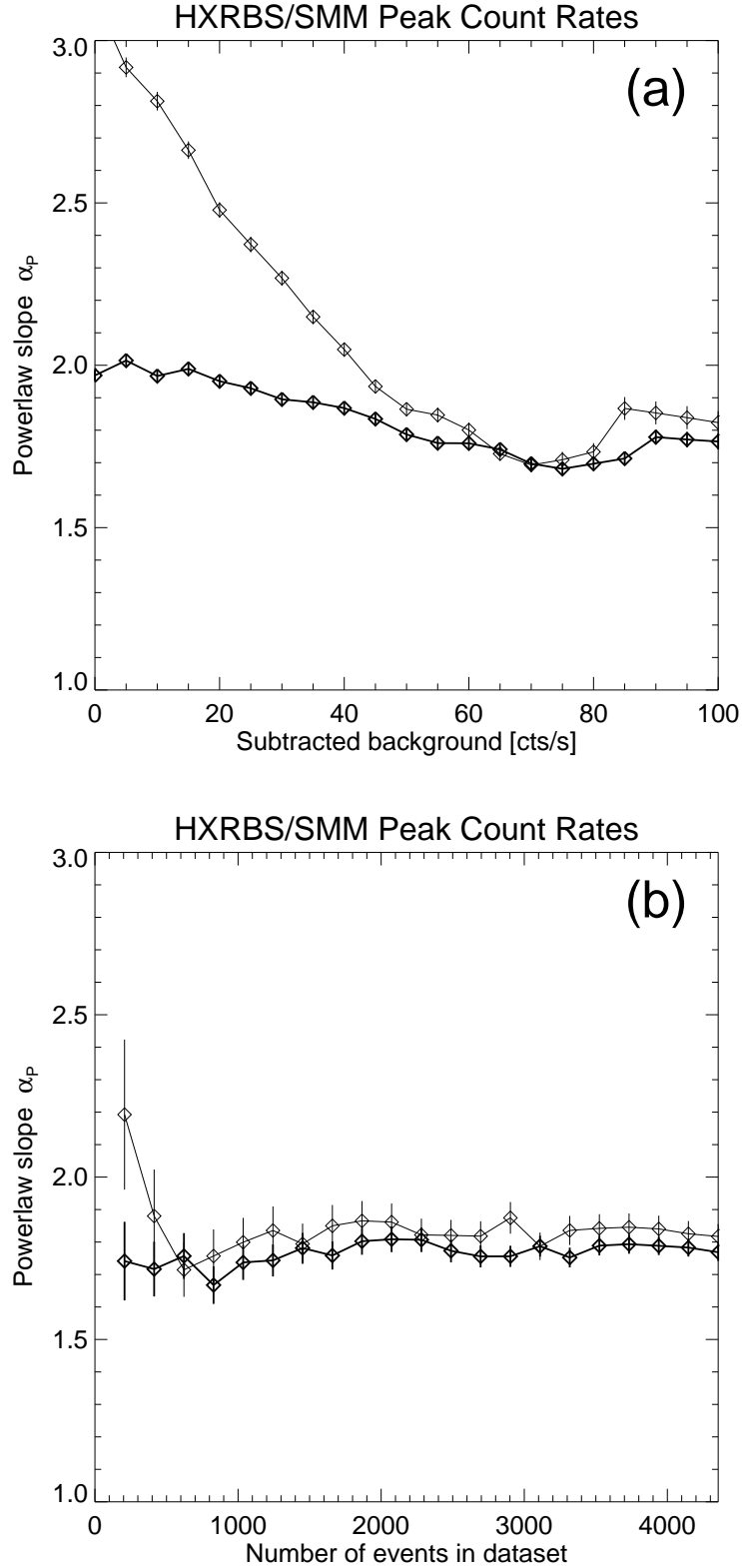


Fig. 13.— The dependence of the power law slope on the amount of subtracted background (a) and on the number of events as a function of time (b) is shown for the cumulative size distribution fits (thick linestyle) and the differential size distribution fits (thin linestyle), for the HXRBS/SMM > 25 keV data set 1980-1982 with 6461 events. A background of 57 cts/s is subtracted in the subsets in (b).

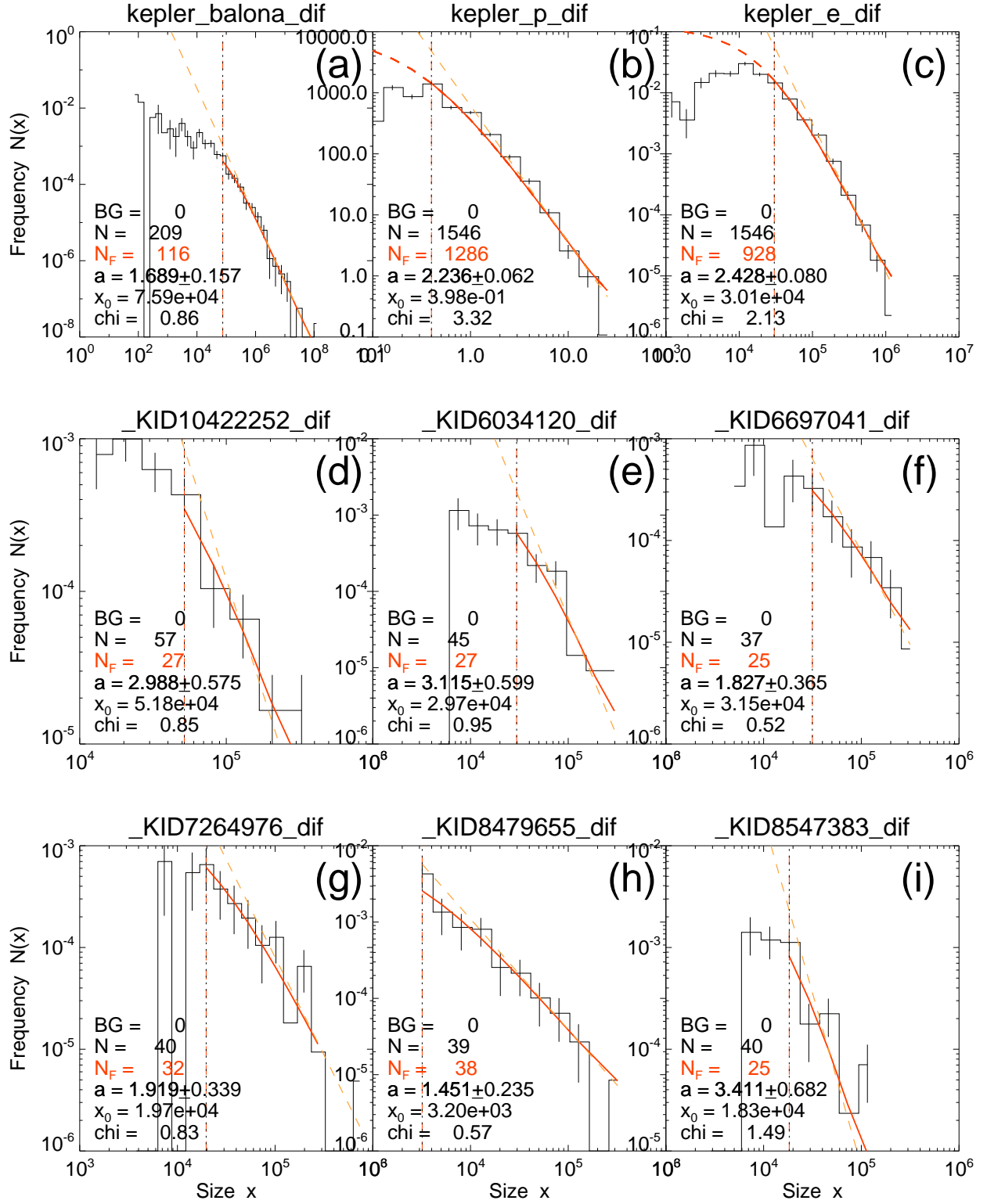


Fig. 14.— Differential size distributions of stellar flares observed from the Kepler mission, described in Balona (2015) and in Shibayama et al. (2013).

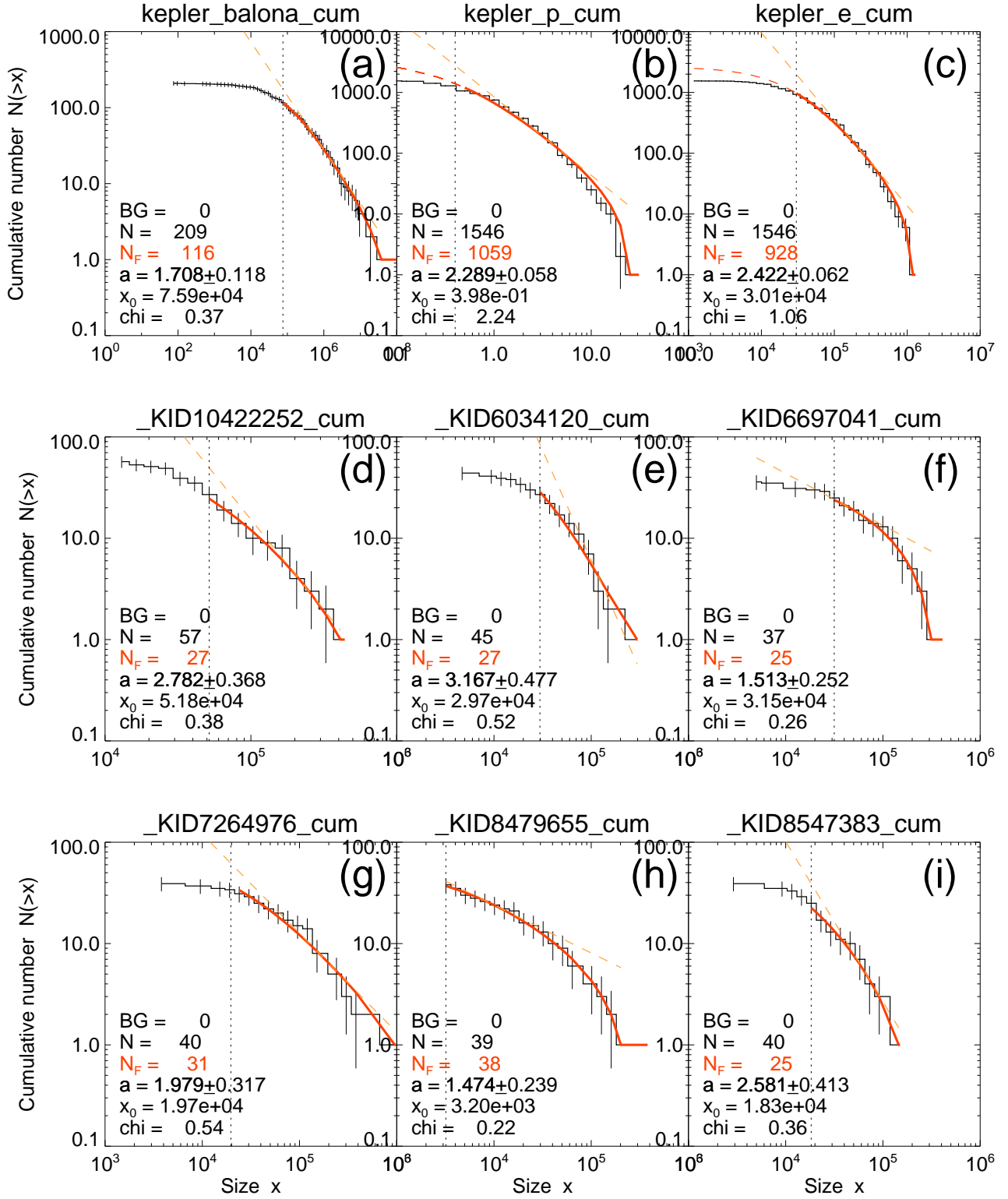


Fig. 15.— Cumulative size distributions of stellar flares observed from the Kepler mission, described in Balona (2015) and in Shibayama et al. (2013).

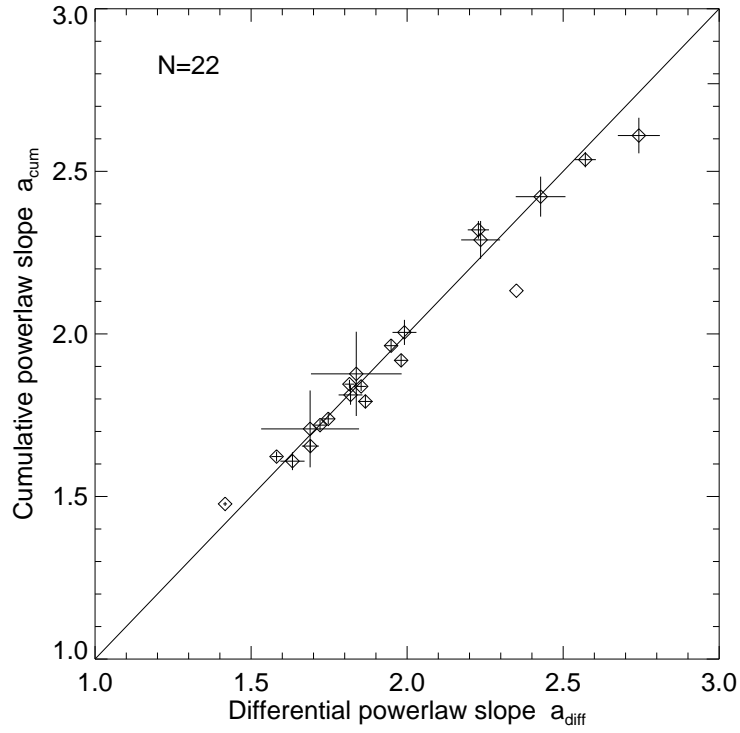


Fig. 16.— The accuracy of the fitted power law slope $\alpha \pm \sigma_\alpha$ is shown as a scatterplot between the differential size distribution fit method (x-axis) and the cumulative size distribution method (y-axis), for the 18 empirical and solar data sets shown in Figures 8–11.